PERGAMON

International Journal of Solids and Structures 37 (2000) 7231–7257

INTERNATIONAL JOURNAL OF SOLIDS and STRUCTURES

www.elsevier.com/locate/ijsolstr

Finite-element analysis of localization of deformation and fluid pressure in an elastoplastic porous medium

Jonas Larsson *, Ragnar Larsson

Department of Solid Mechanics, Chalmers University of Technology, S-412 96 Göteborg, Sweden

Received 18 August 1999; in revised form 22 February 2000

Abstract

The paper concerns the issue of progressive development of shear bands in the problem of coupled deformation and fluid diffusion in porous media. The governing continuum equations are based on porous media theory applied to an elastic–plastic solid skeleton at small deformations. In the localization analysis, the concept of regularized discontinuity is extensively used at the application to the conservation laws of momentum and mass. As a result, we obtain a coupled localization condition that is preserved also in the numerical formulation. Attention is also given to the design of an overall numerical algorithm to solve the coupled set of non-linear finite-element equations that arise from the element-embedded band approach. In order to arrive at the proper design of the algorithm, we resort to a staggering between the continuous (global) problem and the discontinuous (element) problems. In the numerical examples, the algorithm is shown to be able to capture onset of localization as well as the progressive development of shear bands. In the examples, we study the influence of local and global (boundary) drainage conditions, and the internal friction angle to the failure mechanisms.

Keywords: Porous media; Consolidation; Numerical methods; Shear band; Failure; Softening; Stability

1. Introduction

In a two phase porous material, such as fluid saturated soil material, the behavior in the failure situation is influenced by the interaction between the solid and the fluid phase. For example, it is well known that the fluid phase plays an important role in failures in experimental tests, as reported by Han and Vardoulakis (1991), Vardoulakis (1996a,b), Finno et al. (1997) as well as in failures of natural soil slopes (Rankka, 1994; Öberg, 1997; Kirkebø, 1994) and other types of structures involving soil. Hence, for a fully fluid saturated soil this hydro-mechanical coupling is strong and needs to be addressed in the modeling situation. In this context, we note that the two-phase interaction introduces a rate dependency into the problem, although a rate-independent model is used to model the (underlying) effective material. In analogy with viscous

* Corresponding author. Tel.: +46-31-7725269; fax: +46-31-7723826.
E-mail addresses: jonasla@solid.chalmers.se (J. Larsson), ragnar@solid.chalmers.se (R. Larsson).

0020-7683/00/$ - see front matter
PII: S0020-7683(00)00197-9

one-phase regularization (Needleman, 1988), this rate dependency naturally introduces a length scale that may limit the width of the shear band (Loret and Prevost, 1991). However, this "interaction induced regularization" obviously depends strongly on the permeability parameter, and it should therefore not be the sole regularization mechanism in an analysis. Nevertheless, due to the fluid phase interaction, the pathological mesh dependency in the coupled problem may not be so dramatic as in the corresponding single phase situation, as reported by Schrefler et al. (1996, 1998) and Panesso et al. (1998).

To remedy the pathological mesh dependency in the problem, various "localization limiters" have been proposed in the literature. Examples of approaches which preserve the continuity of the deformation fields are rate-dependent visco-plastic, non-local, micro-polar and gradient models. A review of these approaches can be found in De Borst et al. (1993). In contrast to the formulations based on continuous fields, one may augment the conventional continuum with a local regularization that becomes effective only in the post-localized regime. Following the development in the works of Larsson et al. (1993), Simo et al. (1993b), Larsson and Runesson (1996a), this means to introduce a regularized strong discontinuity, which leads to the establishment of cohesive zone type of models, where the regularization preserves the coupling between the pre- and post-localized behavior. Basically, the properties of the cohesive zone, such as the condition for onset of localization and orientation of the localization band, are described by the acoustic tensor. The formulation in the present paper falls within this framework.

Numerical simulations on the hydro-mechanically coupled problem with emphasis on localization is presented in the work by Loret and Prevost (1991). For the continuum model they find that for the occurrence of stationary discontinuities, the localization condition for the porous media is identical to that of the underlaying drained, "effective", material. The discretized problem is regularized using a visco-plastic material model. More recently, Ehlers and Volk (1997), presented a formulation where the problem is regularized with Cosserat theory with which they apparently obtain good results. A possible drawback in these models is the re-meshing procedure that is required in order to resolve the size of the localization zone. This difficulty also carries over to the formulation in Steinmann (1999), where an interface model is suggested on the basis of an interface law for the fluid phase, where the interface fluid supply follows from an assumption for the interface excess pore pressure gradient. Basically, the interface fluid supply is motivated by a "projection" argument of the Darcy law from the continuous to the discontinuous response. A formulation based on strong discontinuities is also proposed in Armero and Callari (1999), where they follow the ideas of Coussy (1995) to assume discontinuities in skeleton displacement and fluid diffusion (fluid content). In this one-dimensional formulation, the assumed discontinuities are embedded into the finite elements.

In the present paper, it is proposed to capture the development of regularized discontinuities in the displacement and pressure fields on the basis of the concept of regularized strong discontinuity (Simo et al., 1993b; Larsson and Runesson, 1996a). In the present case of the two-phase continuum, the concept of regularized discontinuity is extensively exploited at the application to the conservation laws of momentum and mass, as discussed in Larsson and Larsson (2000). As a result, we obtain a localization condition that couples the displacement and pressure discontinuities. On the numerical side, a finite-element (FE) procedure for the mixture of soil and pore fluid is proposed on the basis of the "embedded approach", where the FE interpolation allows for discontinuities within the finite elements. The procedure falls within the range of enhanced assumed strain methods, where the FE equations are derived from a three-field variational formulation, as discussed by Simo and Rifai (1990). From the pertinent orthogonality condition, a coupled set of FE equations are obtained, where the coupling between continuous and discontinuous response is obtained at the element level. In the 4 present formulation, the orthogonality condition preserves traction continuity and continuity of mass balance across the element embedded band in an integrated fashion. Under certain circumstances, the coupled localization condition may be shown to be preserved by the finite-element formulation, and the element response may be characterized like in the continuum situation.

Attention is also given to the design of an overall FE algorithm to solve the coupled set of non-linear FE equations that arise from the element-embedded band approach. The discontinuities are conveniently treated as local element enhancements of the FE interpolations leading to a set of local element equations. In order to arrive at the proper design of the algorithm, we resort to a staggering between the continuous (global) problem and the discontinuous (element) problems. At the application to the numerical examples, the algorithm is shown to work well in terms of its ability to capture onset of localization as well as post-localized regime. In the examples, we study the influence of local (intrinsic permeability) and global (boundary) drainage conditions to the failure mechanisms and also the flow and pressure in the localized zones.

2. Governing equations for elastic–plastic porous media

2.1. Balance equations

The theory of porous media is, here, understood as mixture theory combined with the volume fraction concept. The constituents are denoted c^α, with $\alpha = s$ for the solid and $\alpha = f$ for the fluid phase, and the volume fractions $\xi_\alpha(\mathbf{x}, t)$ are defined as the ratio between the local constituent volume v_α and the bulk mixture volume v. Thereby, the bulk density (per unit bulk volume of mixture) is obtained as $\hat{\rho}_\alpha = \xi_\alpha \rho_\alpha$, where ρ_α is the intrinsic density associated with c^α. We further assume that small deformations are at hand and that each constituent is intrinsically incompressible, i.e., $D_f\rho_f/Dt = D_s\rho_s/Dt := 0$. Moreover, it is assumed that no voids can develop during deformation, whereby the volume fractions must satisfy the saturation constraint $\xi_s + \xi = 1$, where $\xi \equiv \xi_f$ is the porosity and ξ_s the corresponding volume fraction of the soil skeleton. The momentum balance for such a porous media may be stated as follows:

$$\nabla \cdot \bar{\boldsymbol{\sigma}} + \hat{\rho}\mathbf{g} = \mathbf{0}, \tag{1}$$

where $\bar{\boldsymbol{\sigma}}$ is the total stress and $\hat{\rho}$ is the saturated density of the soil fluid mixture. Mass conservation during deformation of the porous medium, is expressed as

$$\nabla \cdot \dot{\mathbf{u}} + \nabla \cdot \mathbf{v}_d = 0, \tag{2}$$

where $\mathbf{v}_d = \xi(\mathbf{v}_f - \mathbf{v}_s) = \xi\mathbf{v}_r$ is the Darcian velocity. We note that $\mathbf{v}_d$ represents the relative volumetric flow of fluid such that $\mathbf{v}_d \cdot \mathbf{n}$ is the volume of fluid passing through a surface following the skeleton with normal $\mathbf{n}$ per time unit.

2.2. Constitutive equations

From thermodynamic arguments, as discussed in Larsson and Larsson (2000), constitutive equations are established for the effective stress $\boldsymbol{\sigma}$ and the effective drag force between constituents arising from the relative movement. In particular, we choose the constitutive equation for the effective drag force such that Darcy's law is recovered, i.e.,

$$\mathbf{v}_d = -k\nabla p, \tag{3}$$

where k is the Darcian permeability coefficient for isotropic permeability and p, the excess fluid (intrinsic) pore pressure. As to the effective stress, we establish the appropriate constitutive relation within the rate-independent plasticity framework. For this purpose, we define the Helmholtz free energy density (per unit volume) as

$$\psi_s(\boldsymbol{\varepsilon}, \boldsymbol{\varepsilon}^p, \kappa) = \tfrac{1}{2}(\boldsymbol{\varepsilon} - \boldsymbol{\varepsilon}^p) : \mathbf{E}^e : (\boldsymbol{\varepsilon} - \boldsymbol{\varepsilon}^p) + \overline{\psi}, \qquad \overline{\psi}(\kappa) = \tfrac{1}{2}H\kappa^2, \tag{4}$$

where $\mathbf{E}^{\mathrm{e}}$ is the elastic stiffness tensor, $\boldsymbol{\varepsilon}$ is the total strain, $\boldsymbol{\varepsilon}^{\mathrm{p}}$ is the total plastic strain, κ is a hardening variable and H denotes the hardening/softening modulus. The equations of state are

$$\boldsymbol{\sigma} = \frac{\partial \psi_{\mathrm{s}}}{\partial \boldsymbol{\varepsilon}} = \mathbf{E}^{\mathrm{e}} : (\boldsymbol{\varepsilon} - \boldsymbol{\varepsilon}^{\mathrm{p}}), \qquad K = -\frac{\partial \psi_{\mathrm{s}}}{\partial \kappa} = -H\kappa, \tag{5}$$

where K is the dissipative stress conjugated to κ. Furthermore, we introduce the convex, but not necessarily smooth, set $\mathscr{B}$ of admissible states:

$$\mathscr{B} = \{\boldsymbol{\sigma}, K : \varphi(\boldsymbol{\sigma}, K) \leqslant 0\}, \tag{6}$$

where $\varphi(\boldsymbol{\sigma}, K) = 0$ is the state boundary surface. Constitutive rate equations for $\boldsymbol{\varepsilon}^{\mathrm{p}}$ and κ are defined via the evolution rules:

$$\dot{\boldsymbol{\varepsilon}}^{\mathrm{p}} = \dot{\lambda}\frac{\partial \varphi^*}{\partial \boldsymbol{\sigma}}, \qquad \dot{\kappa} = -\dot{\lambda}\frac{\partial \varphi}{\partial K}, \tag{7}$$

where λ is the plastic multiplier which is determined from the Kuhn–Tucker conditions:

$$\dot{\lambda} \geqslant 0, \quad \varphi \leqslant 0, \quad \dot{\lambda}\varphi = 0. \tag{8}$$

In Eq. (7), we have included the possibility of a non-associated plastic flow through the plastic potential function φ^*. From the condition of linearized (un)loading it may be shown in a standard fashion that the linearized response for the effective stress can be written as

$$\dot{\boldsymbol{\sigma}} = \mathbf{E} : \dot{\boldsymbol{\varepsilon}}, \qquad \mathbf{E} = \begin{cases} \mathbf{E}^{\mathrm{ep}} = \mathbf{E}^{\mathrm{e}} - \frac{1}{h}\mathbf{E}^{\mathrm{e}} : \mathbf{f}^* \otimes \mathbf{f} : \mathbf{E}^{\mathrm{e}} & (\mathrm{P}), \\ \mathbf{E}^{\mathrm{e}} & (\mathrm{E}), \end{cases} \tag{9}$$

where $\mathbf{f} := \partial\varphi/\partial\boldsymbol{\sigma}$ and $\mathbf{f}^* := \partial\varphi^*/\partial\boldsymbol{\sigma}$ and (P) and (E) denote plastic and elastic loading, respectively. Moreover, the plastic modulus h is defined as $h = \mathbf{f} : \mathbf{E}^{\mathrm{e}} : \mathbf{f}^* + H$.

3. Regularized discontinuous fields in a porous medium

3.1. Concept of regularized discontinuous fields

Our aim is to develop a FE formulation that can handle the existence of a discontinuity for the hydro-mechanically coupled problem described above. To this end, let us consider the possibility for the existence of a regularized discontinuity the displacement and the excess pore pressure fields of the coupled problem Fig. 1. We follow the developments in Larsson and Larsson (2000), where the concept of regularized

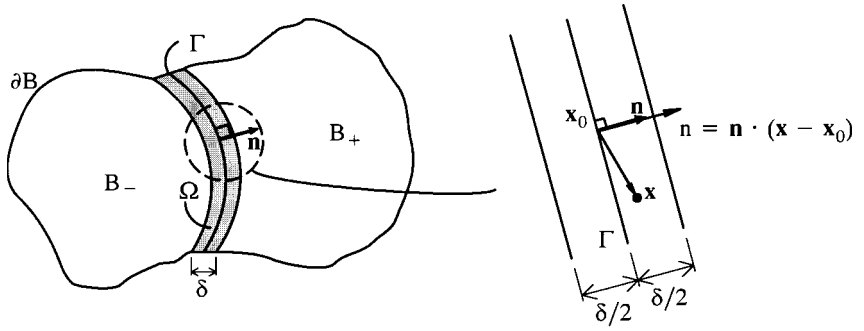

Fig. 1. Body B with boundary ∂B divided by a characteristic surface Γ. The regularization band Ω of width δ is centered on Γ.

discontinuity is extensively exploited. In brief, this means to introduce a band of width δ to construct regularized derivatives of the Heaviside function. These regularized functions are consistent in the sense that they describe qualitatively the true derivatives in a distributional sense as δ tends to zero. Hence, the length δ should be small in relation to a characteristic dimension of the structure. In practice, the lower limit of δ is bounded by the computer precision. We note that the present formulation based on the concept of regularized strong discontinuities becomes related to the formulation of Rudnicki (1983). The essential difference is the introduction of a length scale, and that we do not consider a priori a zone of weakened material.

We assume that the discontinuities occurs across the internal surface Γ with unit normal $\mathbf{n}$. This surface sub-divides B into the sub-domains B_- and B_+ in such a way that $\mathbf{n}$ is pointing from B_- to B_+, as shown in Fig. 1. It is then assumed that the velocity field of the skeleton takes on the structure:

$$\dot{\mathbf{u}}(\mathbf{x},\mathrm{t}) = \dot{\mathbf{u}}_{\mathrm{c}}(\mathbf{x},\mathrm{t}) + [\![\dot{\mathbf{u}}]\!](\mathbf{t})\mathrm{H}_\Gamma(\mathbf{x}), \tag{10}$$

where $\mathbf{u}_{\mathrm{c}}$ is the continuous portion of the skeleton displacement and $[\![\dot{\mathbf{u}}]\!]$ is the spatially constant jump of $\mathbf{u}$ across Γ. Moreover, H_Γ is the Heaviside function defined as

$$\mathrm{H}_\Gamma = \begin{cases} 0 & \text{if } \mathbf{x} \in B_-, \\ 1 & \text{if } \mathbf{x} \in B_+. \end{cases} \tag{11}$$

In order to regularize the Dirac delta distribution $\boldsymbol{\delta}_\Gamma = \nabla H_\Gamma$, which has meaning only in a distributional sense, we introduce a thin zone $\Omega \subset B$ along Γ with the width δ, as shown in Fig. 1. Within this zone we define $\mathbf{x}_0 \in \Gamma$ and $\mathbf{x} \in \Omega$ such that $\mathbf{x} = \mathbf{x}_0 + n\mathbf{n}$ (with $-\delta/2 \leqslant n \leqslant \delta/2$). The strictly discontinuous Heaviside function is then replaced by a ramp function in the coordinate n, whereby the regularized function $\boldsymbol{\delta}_{\Gamma,\mathrm{r}}$ is expressed as

$$\boldsymbol{\delta}_{\Gamma,\mathrm{r}} = \frac{f(n)}{\delta}\mathbf{n} \quad \text{with } f(n(\mathbf{x})) = \begin{cases} 1 & \text{if } \mathbf{x} = \mathbf{x}_0 \in \Gamma, \\ 0 & \text{if } \mathbf{x} = \mathbf{x}_\pm \in B \setminus \Gamma. \end{cases} \tag{12}$$

Let us also consider the regularization of the divergence $\nabla \cdot \boldsymbol{\delta}_{\Gamma,\mathrm{r}}$ and the gradient $\nabla(\nabla \cdot \boldsymbol{\delta}_{\Gamma,\mathrm{r}})$. We then regularize the function $f(n)$ based on the dashed linear functions across Ω indicated in Fig. 2a. As a result, we obtain from Eq. (12) the relation,

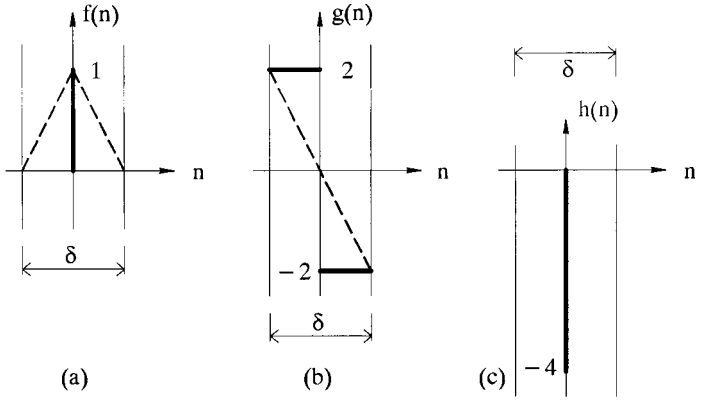

Fig. 2. (a–c) Functions f, g and h as the result of successive regularizations.

$$\nabla \cdot \boldsymbol{\delta}_{\Gamma,\mathrm{r}} := \frac{1}{\delta^2} g(n) \quad \text{with } g(n(\mathbf{x})) = \begin{cases} 2 & \text{if } \mathbf{x} = \mathbf{x}_- \in B_- \setminus \Gamma, \\ -2 & \text{if } \mathbf{x} = \mathbf{x}_+ \in B_+ \setminus \Gamma, \\ 0 & \text{otherwise.} \end{cases} \tag{13}$$

As to the term $\nabla(\nabla \cdot \boldsymbol{\delta}_{\Gamma,\mathrm{r}})$, we regularize the function $g(n)$ based on Fig. 2b and Eq. (13), whereby we obtain

$$\nabla(\nabla \cdot \boldsymbol{\delta}_{\Gamma,\mathrm{r}}) := \frac{1}{\delta^3} h(n)\mathbf{n} \quad \text{with } h(n(\mathbf{x})) = \begin{cases} -4 & \text{if } \mathbf{x} = \mathbf{x}_0 \in \Gamma, \\ 0 & \text{if } \mathbf{x} = \mathbf{x}_\pm \in B \setminus \Gamma. \end{cases} \tag{14}$$

We are now in the position to express the strain rate $\dot{\boldsymbol{\varepsilon}}$ pertient to the proposed regularization. Hence, in view of Eqs. (10) and (12), we obtain

$$\dot{\boldsymbol{\varepsilon}} = (\nabla \otimes \dot{\mathbf{u}})^{\mathrm{sym}} = \dot{\boldsymbol{\varepsilon}}_{\mathrm{c}} + \frac{f}{\delta}(\mathbf{n} \otimes [\![\dot{\mathbf{u}}]\!])^{\mathrm{sym}}, \quad \dot{\boldsymbol{\varepsilon}}_{\mathrm{c}} = (\nabla \otimes \dot{\mathbf{u}}_{\mathrm{c}})^{\mathrm{sym}}. \tag{15}$$

Moreover, upon invoking Eq. (15) into the constitutive relation (9), we find that the effective stress rate field $\dot{\boldsymbol{\sigma}}$ take the structure,

$$\dot{\boldsymbol{\sigma}} = \dot{\boldsymbol{\sigma}}_{\mathrm{c}} + f[\![\dot{\boldsymbol{\sigma}}]\!] \quad \text{with } [\![\dot{\boldsymbol{\sigma}}]\!] = \dot{\boldsymbol{\sigma}}(\mathbf{x}_0) - \dot{\boldsymbol{\sigma}}(\mathbf{x}_\pm), \tag{16}$$

where

$$\dot{\boldsymbol{\sigma}}_{\mathrm{c}} = \mathbf{E}(\mathbf{x}_\pm) : \dot{\boldsymbol{\varepsilon}}_{\mathrm{c}}, \qquad [\![\dot{\boldsymbol{\sigma}}]\!] = [\![\mathbf{E}]\!] : \dot{\boldsymbol{\varepsilon}}_{\mathrm{c}} + \frac{1}{\delta}(\mathbf{E}(\mathbf{x}_0) \cdot \mathbf{n}) \cdot [\![\dot{\mathbf{u}}]\!]. \tag{17}$$

In Eq. (17), we remark that $[\![\dot{\boldsymbol{\sigma}}]\!]$ denotes the consequent jump of the stress rate due to the constitutive response and the regularized displacement discontinuity. Moreover, we introduced $[\![\mathbf{E}]\!] = \mathbf{E}(\mathbf{x}_0) - \mathbf{E}(\mathbf{x}_\pm)$ as the jump in the tangent stiffness. We note that $\mathbf{E}(\mathbf{x}_0)$ and $\mathbf{E}(\mathbf{x}_\pm)$ are generally different, i.e., ($\mathbf{E}^{\mathrm{e}}$ or $\mathbf{E}^{\mathrm{ep}}$), depending on whether elastic or plastic loading takes place.

As to the fluid pore pressure, we are guided by the effective stress principle, i.e., $\bar{\boldsymbol{\sigma}} = \boldsymbol{\sigma} - p\mathbf{1}$, to adopt the crucial assumption that p has the same structure as the effective stress field. We thus assume

$$\dot{p} = \dot{p}_{\mathrm{c}} + f[\![\dot{p}]\!] \quad \text{with } [\![\dot{p}]\!] = \dot{p}(\mathbf{x}_0) - \dot{p}(\mathbf{x}_\pm), \tag{18}$$

where p_{c} is the continuous portion of the pressure field. The possible development of a jump in pressure in the post-localized regime may also be regarded as a consequence of mass balance. That is, for the mass balance Eq. (2) to be satisfied, the term $\nabla \cdot \mathbf{v}_{\mathrm{d}}$ must have an identical structure as the volumetric skeleton strain. If the Darcy law is employed, this in turn requires the chosen structure of the pore pressure in Eq. (18). Hence, by combining Eqs. (17) and (18), the total stress rate field $\dot{\bar{\boldsymbol{\sigma}}}$ can be written

$$\dot{\bar{\boldsymbol{\sigma}}} = \dot{\bar{\boldsymbol{\sigma}}}_{\mathrm{c}} + f[\![\dot{\bar{\boldsymbol{\sigma}}}]\!], \tag{19}$$

where

$$\dot{\bar{\boldsymbol{\sigma}}}_{\mathrm{c}} = \dot{\boldsymbol{\sigma}}_{\mathrm{c}} - \dot{p}_{\mathrm{c}}\mathbf{1}, \qquad [\![\dot{\bar{\boldsymbol{\sigma}}}]\!] = [\![\dot{\bar{\boldsymbol{\sigma}}}]\!] - [\![\dot{p}]\!]\mathbf{1}. \tag{20}$$

Moreover, from Eqs. (3) and (18), it follows that the Darcian velocity has the structure,

$$\mathbf{v}_{\mathrm{d}} = \mathbf{v}_{\mathrm{d,c}} + g[\![\mathbf{v}_{\mathrm{d}}]\!] \quad \text{with } \mathbf{v}_{\mathrm{d,c}} = -k\nabla p_{\mathrm{c}} \quad \text{and } [\![\mathbf{v}_{\mathrm{d}}]\!] = -\frac{k}{\delta}[\![p]\!]\mathbf{n}. \tag{21}$$

We note that the assumption about a discontinuous pressure in the present formulation differs from the work of Armero and Callari (1999). In their formulation truly discontinuous fields are chosen for the displacement and the fluid flow. Across the discontinuity surface the pressure field is chosen continuous.

3.2. Condition for the existence of regularized strong discontinuity

In order to establish the conditions that must be satisfied in order for a strong discontinuity to appear, we consider the continuity of the momentum and mass conservation relations, as expressed in Eqs. (1) and (2).

Assuming that the body force is continuous, it must be required due to linear momentum conservation that

$$\nabla \cdot \dot{\bar{\boldsymbol{\sigma}}}|_{\mathbf{x}=\mathbf{x}_\pm} - \nabla \cdot \dot{\bar{\boldsymbol{\sigma}}}|_{\mathbf{x}=\mathbf{x}_0} = \mathbf{0} \tag{22}$$

which leads to the (usual) traction continuity condition:

$$\mathbf{n} \cdot [\![\dot{\bar{\boldsymbol{\sigma}}}]\!] = \mathbf{0}. \tag{23}$$

Likewise, we formulate the condition for continuity of the mass conservation across Γ in terms of Eq. (2) as

$$(\nabla \cdot \dot{\mathbf{u}} + \nabla \cdot \mathbf{v}_\mathrm{d})|_{\mathbf{x}=\mathbf{x}_\pm} - (\nabla \cdot \dot{\mathbf{u}} + \nabla \cdot \mathbf{v}_\mathrm{d})|_{\mathbf{x}=\mathbf{x}_0} = 0 \tag{24}$$

which yields

$$-\frac{f}{\delta}\mathbf{n} \cdot [\![\dot{\mathbf{u}}]\!] - \frac{h}{\delta}\mathbf{n} \cdot [\![\mathbf{v}_\mathrm{d}]\!] = 0. \tag{25}$$

Finally, on introducing Eq. (20) into Eq. (23) and Eq. (21) into Eq. (24), we obtain a localization condition (= condition for the existence of regularized discontinuities) that represents momentum and mass conservation for our porous material as follows:

$$\begin{aligned} &\frac{1}{\delta}\mathbf{Q}_\Gamma \cdot [\![\dot{\mathbf{u}}]\!] - [\![\dot{p}]\!]\mathbf{n} = -\mathbf{n} \cdot [\![\mathbf{E}]\!] : \dot{\boldsymbol{\varepsilon}}_\mathrm{c}, \\ &\mathbf{n} \cdot [\![\dot{\mathbf{u}}]\!] - 4\mathbf{n} \cdot [\![\mathbf{v}_\mathrm{d}]\!] = 0. \end{aligned} \tag{26}$$

We emphasize that this condition must be satisfied at the onset of localization as well as in the post-localized range. In Eq. (26), we introduced $\mathbf{Q}_\Gamma$ as the acoustic tensor associated with the effective material, i.e., $\mathbf{Q}_\Gamma = \mathbf{n} \cdot \mathbf{E}(\mathbf{x}_0) \cdot \mathbf{n}$.

A thorough investigation of condition (26) is carried out in Larsson and Larsson (2000). It turns out that when the underlying drained material signals localization, an unstable situation is at hand where an imperfection causes growth of pressure and displacement discontinuities. Consequently, singularity of $\mathbf{Q}_\Gamma$ is taken as the proper localization condition in the coupled situation. To this end, it should be noted that the predictions of Eq. (26) are closely related to the ones presented in Rudnicki (1983). Other contributions that have arrived at the conclusion that it is the drained localization condition that signals localization in the coupled case are Rice (1975) and Loret and Prevost (1991). In contrast to these findings, Benallal and Comi (1997) study the condition for loss of ellipticity of the time-discretized initial boundary value problem. Here, the condition for ill-posedness is derived by seeking equal wave form solutions of the displacement and pore pressure. In the case of explicit forward integration, which essentially corresponds to a rate analysis, the conclusion is that loss of ellipticity occurs for singularity of the undrained acoustic tensor.

4. Mixed weak formulation with embedded discontinuities

We consider the weak formulation for a domain B with external boundary ∂B which is occupied by fluid saturated porous material. The external boundary, with outward unit normal $\bar{\mathbf{n}}$, is divided into two parts in two different ways. On one hand, the boundary ∂B is divided into two mutually exclusive parts $\partial_\mathrm{u} B$

(prescribed skeleton displacement) and $\partial_t B$ (prescribed total traction) such that $\partial_u B \cup \partial_t B = \partial B$. On the other hand, ∂B is divided into two mutually exclusive parts $\partial_p B$ (prescribed pore fluid pressure) and $\partial_q B$ (prescribed fluid volume flux) such that $\partial_p B \cup \partial_q B = \partial B$. For the establishment of weak equations incorporating embedded discontinuities in displacement and pressure, we generalize the developments in Larsson et al. (1996) for the undrained continuum to the partly drained situation. In the sequel below, the enhanced strain approach is the key feature, which was originally proposed by Simo and Rifai (1990). To this end, let U, P_c be the spaces of admissible displacement and pressure variations, defined in a standard fashion as

$$\begin{aligned} U &:= \{\mathbf{u}'_c \in H^1(B) : \mathbf{u}'_c = \mathbf{0} \text{ on } \partial_u B\}, \\ P_c &:= \{p'_c \in H^1(B) : p'_c = 0 \text{ on } \partial_p B\}. \end{aligned} \tag{27}$$

Further, we shall denote by E, E_v, S, V, P, and N the spaces of admissible strain, volumetric strain, effective stress, Darcian velocity, pressure and pressure gradient, respectively. In particular, we may set tentatively

$$E = E_v = S = V = P = N := L_2(B). \tag{28}$$

The sets of weak equations are then proposed as follows:

$$\begin{aligned} &\int_B \boldsymbol{\varepsilon}'_c : \boldsymbol{\tau}\, d\Omega - W_u^{ext}(\mathbf{u}'_c) = 0, \quad \boldsymbol{\varepsilon}'_c = (\nabla \otimes \mathbf{u}'_c)^{sym} \quad \forall \mathbf{u}'_c \in U, \\ &\int_B \boldsymbol{\tau}' : (\boldsymbol{\varepsilon}_c - \boldsymbol{\varepsilon})\, d\Omega = 0 \quad \forall \boldsymbol{\tau}' \in S, \\ &\int_B \boldsymbol{\varepsilon}' : (-\boldsymbol{\tau} + \boldsymbol{\sigma} - p\mathbf{1})\, d\Omega = 0 \quad \forall \boldsymbol{\varepsilon}' \in E, \end{aligned} \tag{29}$$

$$\begin{aligned} &\int_B \boldsymbol{\eta}'_c \cdot \mathbf{w}\, d\Omega - \int_B p'_c \dot{\gamma}\, d\Omega - W_p^{ext}(p'_c) = 0 \quad \forall p'_c \in P_c \;\; \boldsymbol{\eta}'_c = \nabla p'_c, \\ &\int_B \gamma'(p_c - p)\, d\Omega = 0 \quad \forall \gamma' \in E_v, \\ &\int_B \mathbf{w}' \cdot (\boldsymbol{\eta}_c - \boldsymbol{\eta})\, d\Omega = 0 \quad \forall \mathbf{w}' \in V, \\ &\int_B \boldsymbol{\eta}' \cdot (-\mathbf{w} + \mathbf{v}_d)\, d\Omega - \int_B p'(-\dot{\gamma} + \dot{\varepsilon}_v)\, d\Omega = 0 \quad \forall p' \in P \;\; \forall \boldsymbol{\eta}' = \nabla p' \in N. \end{aligned} \tag{30}$$

Here, Eq. (29) represents the balance of linear momentum, where $\boldsymbol{\tau}$ is the total stress field and $\boldsymbol{\varepsilon}$, the total strain field. Eq. (30) represents the balance of mass where γ is the volumetric strain field; $\mathbf{w}$, the relative fluid flow; $\boldsymbol{\eta}$, the total pressure gradient and $\varepsilon_v = \mathrm{tr}(\boldsymbol{\varepsilon})$. The external virtual work quantities are given by

$$\begin{aligned} W_u^{ext}(\mathbf{u}'_c) &= \int_B \mathbf{u}'_c \cdot \hat{\rho}\mathbf{g}\, d\Omega + \int_{\partial_t B} \mathbf{u}'_c \cdot \bar{\mathbf{t}}\, d\Gamma, \\ W_p^{ext}(p'_c) &= \int_{\partial_q B} p'_c \bar{q}\, d\Gamma, \end{aligned} \tag{31}$$

where $\bar{q} = \mathbf{v}_d \cdot \bar{\mathbf{n}}$ is the fluid volume flux (outflow) and $\bar{\mathbf{t}} = \bar{\boldsymbol{\sigma}} \cdot \bar{\mathbf{n}}$, the total prescribed traction, with $\bar{\mathbf{n}}$ being the outward unit normal of ∂B.

The variational fields $\boldsymbol{\varepsilon}' \in E, p' \in P$ and $\boldsymbol{\eta}' \in N$ are considered decomposed into the structure:

$$\begin{aligned} &\boldsymbol{\varepsilon}' = \boldsymbol{\varepsilon}'_c + \tilde{\boldsymbol{\varepsilon}}' \in U \times \tilde{E} \quad \text{with } \boldsymbol{\varepsilon}'_c = (\nabla \otimes \mathbf{u}'_c)^{sym}, \\ &p' = p'_c + \tilde{p}' \in P_c \times \tilde{P}, \\ &\boldsymbol{\eta}' = \boldsymbol{\eta}'_c + \tilde{\boldsymbol{\eta}}' \in \nabla P_c \times \tilde{N} \quad \text{with } \boldsymbol{\eta}'_c = \nabla p_c, \end{aligned} \tag{32}$$

where $\tilde{\boldsymbol{\varepsilon}}' \in \tilde{E}$ represents the enhanced portion of the total strain. As to the enhanced quantities in Eq. (32), we are guided by Eqs. (15) and (18) to define $\tilde{\boldsymbol{\varepsilon}}' \in \tilde{E}$, $\tilde{p}' \in \tilde{P}$ and $\tilde{\boldsymbol{\eta}}' \in \tilde{N}$ as

$$\begin{aligned} \tilde{\boldsymbol{\varepsilon}}' &= \tilde{\boldsymbol{\varepsilon}}'_{\mathrm{c}} + \delta_\Gamma(\mathbf{n} \otimes \mathbf{v}')^{\mathrm{sym}}, \\ \tilde{p}' &= \tilde{p}'_{\mathrm{c}} + \delta_\Gamma q', \\ \tilde{\boldsymbol{\eta}}' &= \tilde{\boldsymbol{\eta}}'_{\mathrm{c}} + \nabla(\delta_\Gamma q'). \end{aligned} \tag{33}$$

Here, $\mathbf{v}'$ is a displacement-like discontinuity and q', a pressure-like discontinuity (defined per unit internal surface Γ). We note that these expressions have meaning only in a distributional sense. Upon introducing the decompositions (32) and (33) into Eqs. (29) and (30), the weak form of momentum balance, kinematic compatibility and constitutive compatibility is obtained as

$$\int_B \boldsymbol{\varepsilon}'_{\mathrm{c}} : (\boldsymbol{\sigma}(\boldsymbol{\varepsilon}) - p\mathbf{1})\,\mathrm{d}\Omega - W_{\mathrm{u}}^{\mathrm{ext}}(\mathbf{u}') = 0 \quad \forall \mathbf{u}'_{\mathrm{c}} \in U, \tag{34a}$$

$$\int_B \boldsymbol{\tau}' : \tilde{\boldsymbol{\varepsilon}}\,\mathrm{d}\Omega = 0, \quad \forall \boldsymbol{\tau}' \in S, \tag{34b}$$

$$\int_B \tilde{\boldsymbol{\varepsilon}}' : (-\boldsymbol{\tau} + \boldsymbol{\sigma}(\boldsymbol{\varepsilon}) - p\mathbf{1})\,\mathrm{d}\Omega = 0, \quad \forall \tilde{\boldsymbol{\varepsilon}}' \in \tilde{E}. \tag{34c}$$

Similarly, the weak form of mass balance, weak format of compatibility of fluid pressure field, weak format of constitutive compatibility is given by

$$\int_B \boldsymbol{\eta}'_{\mathrm{c}} \cdot \mathbf{v}_{\mathrm{d}}\,\mathrm{d}\Omega - \int_B p'_{\mathrm{c}}\dot{\varepsilon}_{\mathrm{v}}\,\mathrm{d}\Omega - W_{\mathrm{p}}^{\mathrm{ext}}(p'_{\mathrm{c}}) = 0, \quad \forall p'_{\mathrm{c}} \in P_{\mathrm{c}}, \tag{35a}$$

$$\int_B \gamma' \tilde{p}\,\mathrm{d}\Omega = 0, \quad \forall \gamma' \in E_{\mathrm{v}}, \tag{35b}$$

$$\int_B \mathbf{w}' \cdot \tilde{\boldsymbol{\eta}}\,\mathrm{d}\Omega = 0, \quad \forall \mathbf{w}' \in V, \tag{35c}$$

$$\int_B \tilde{\boldsymbol{\eta}}' \cdot (-\mathbf{w} + \mathbf{v}_{\mathrm{d}})\,\mathrm{d}\Omega - \int_B \tilde{p}'(-\dot{\gamma} + \dot{\varepsilon}_{\mathrm{v}})\,\mathrm{d}\Omega = 0, \quad \forall \tilde{\boldsymbol{\eta}}' \in \tilde{N},\ \forall \tilde{p}' \in \tilde{P}. \tag{35d}$$

Pertinent to the enhanced strain approach, we choose S and $\tilde{E}$, E_V and $\tilde{P}$, as well as V and $\tilde{N}$ orthogonal in $L_2(\Omega)$. This leads to

$$\int_B \boldsymbol{\tau}' : \tilde{\boldsymbol{\varepsilon}}'\,\mathrm{d}\Omega \equiv 0 \quad \forall \boldsymbol{\tau}' \in S\ \forall \tilde{\boldsymbol{\varepsilon}}' \in \tilde{E}, \tag{36a}$$

$$\int_B \gamma' \tilde{p}'\,\mathrm{d}\Omega \equiv 0 \quad \forall \gamma' \in E_v\ \forall \tilde{p}' \in \tilde{P}, \tag{36b}$$

$$\int_B \mathbf{w}' \cdot \tilde{\boldsymbol{\eta}}'\,\mathrm{d}\Omega \equiv 0 \quad \forall \mathbf{w}' \in V\ \forall \tilde{\boldsymbol{\eta}} \in \tilde{N}. \tag{36c}$$

We now conclude that Eqs. (34b), (35b) and (35c) are identically satisfied. This means that $\boldsymbol{\tau}$, γ and $\mathbf{w}$ may be eliminated in Eqs. (34c) and (35d), respectively. Hence, we may rephrase the equilibrium equation (34) as

$$\int_B \boldsymbol{\varepsilon}'_{\mathrm{c}} : (\boldsymbol{\sigma}(\boldsymbol{\varepsilon}) - p\mathbf{1})\,\mathrm{d}\Omega - W_{\mathrm{u}}^{\mathrm{ext}}(\mathbf{u}'_{\mathrm{c}}) = 0 \quad \forall \mathbf{u}'_{\mathrm{c}} \in U, \tag{37a}$$

$$\int_B \tilde{\boldsymbol{\varepsilon}}' : (\boldsymbol{\sigma}(\boldsymbol{\varepsilon}) - p\mathbf{1})\,\mathrm{d}\Omega = 0 \quad \forall \tilde{\boldsymbol{\varepsilon}}' \in \tilde{E}, \tag{37b}$$

In the same fashion, using the orthogonality conditions (36a)–(36c), the mass balance (35a)–(35d) is re-written as

$$\int_B \boldsymbol{\eta}'_{\mathrm{c}} \cdot \mathbf{v}_{\mathrm{d}}\,\mathrm{d}\Omega - \int_B p'_{\mathrm{c}} \dot{\varepsilon}_{\mathrm{v}}\,\mathrm{d}\Omega - W_{\mathrm{p}}^{\mathrm{ext}}(p'_{\mathrm{c}}) = 0 \quad \forall p'_{\mathrm{c}} \in P_{\mathrm{c}}, \tag{38a}$$

$$\int_B \tilde{\boldsymbol{\eta}}' \cdot \mathbf{v}_{\mathrm{d}}\,\mathrm{d}\Omega - \int_B \tilde{p}' \dot{\varepsilon}_{\mathrm{v}}\,\mathrm{d}\Omega = 0 \quad \forall \tilde{\boldsymbol{\eta}}' \in \tilde{N},\ \forall \tilde{p}' \in \tilde{P}. \tag{38b}$$

5. Finite-element procedure

5.1. Finite-element formulation

The region B is considered discretized into FEs $\Omega_e, e = 1, \ldots,$ NEL. For a specific element, the compatible displacement and fluid pressure fields along with the appropriate gradients are interpolated by using the standard compatible shape functions, i.e.,

$$\begin{aligned} \mathbf{u}_{\mathrm{c}e} &= \sum_{I=1}^{\mathrm{NOEL}} N_{\mathrm{u}}^I \hat{\mathbf{u}}_e^I, \qquad \boldsymbol{\varepsilon}_{\mathrm{c}e} = (\mathbf{u}_{\mathrm{c}e} \otimes \boldsymbol{\nabla})^{\mathrm{sym}} = \sum_{I=1}^{\mathrm{NOEL}} (\hat{\mathbf{u}}_e^I \otimes \mathbf{m}_{\mathrm{u}}^I)^{\mathrm{sym}} \quad \text{with } \mathbf{m}_{\mathrm{u}}^I = \boldsymbol{\nabla} N_{\mathrm{u}}^I, \\ p_{\mathrm{c}e} &= \sum_{I=1}^{\mathrm{NOEL}} N_{\mathrm{p}}^I \hat{p}_e^I, \qquad \boldsymbol{\eta}_{\mathrm{c}e} = \boldsymbol{\nabla} p_{\mathrm{c}e} = \sum_{I=1}^{\mathrm{NOEL}} \hat{p}_e^I \mathbf{m}_{\mathrm{p}}^I \quad \text{with } \mathbf{m}_{\mathrm{p}}^I = \boldsymbol{\nabla} N_{\mathrm{p}}^I, \end{aligned} \tag{39}$$

where N_{u}^I and $\hat{\mathbf{u}}_e^I$ are the (displacement) shape function and nodal displacement of node I of the element, respectively. Likewise, N_{p}^I and $\hat{p}_e^I$ are the (pressure) shape function and nodal pressure of node I of the element, respectively. In the following, we shall as base element restrict to a triangular element with quadratic shape functions for the displacement and linear for the pressure i.e., NOEL $= 6, 3$ for the displacement and pressure, respectively (Fig. 3).

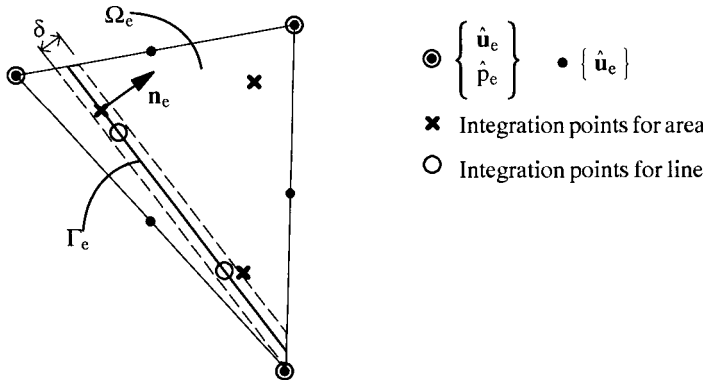

Fig. 3. Enhanced mixed triangular element. The base element has quadratic interpolation for displacement and linear for pressure. The enhanced fields are piecewise constant.

5.1.1. Momentum balance

The FE approximation of $\tilde{\boldsymbol{\varepsilon}}$ and $\boldsymbol{\tau}$ is proposed as

$$\boldsymbol{\tau} = \sum_{e=1}^{\mathrm{NEL}} \chi_e \boldsymbol{\tau}_e, \qquad \tilde{\boldsymbol{\varepsilon}}_{\mathrm{c}} = \sum_{e=1}^{\mathrm{NEL}} \chi_e \tilde{\boldsymbol{\varepsilon}}_{\mathrm{c}e}, \qquad \mathbf{v} = \sum_{e=1}^{\mathrm{NEL}} \chi_e \mathbf{v}_e, \tag{40}$$

where χ_e is defined as

$$\chi_e = \begin{cases} 1 & \text{if } \mathbf{x} \in \Omega_e, \\ 0 & \text{otherwise.} \end{cases} \tag{41}$$

In particular, we consider the choice that the quantities related to the enhanced strain be piecewise constant within each Ω_e such that $\boldsymbol{\tau}_e$ is a constant. Upon inserting these FE-approximations into Eqs. (36a) and (37b), we obtain the "orthogonality" condition that must be satisfied elementwise:

$$\int_{\Omega_e} \tilde{\boldsymbol{\varepsilon}}'_{\mathrm{c}e} : \boldsymbol{\tau}'_e \,\mathrm{d}\Omega + \int_{\Gamma_e} (\mathbf{n}_e \otimes \mathbf{v}'_e)^{\mathrm{sym}} : \boldsymbol{\tau}'_e \,\mathrm{d}\Gamma = 0, \quad e = 1, \ldots, \mathrm{NEL}, \tag{42a}$$

$$\int_{\Omega_e} \tilde{\boldsymbol{\varepsilon}}'_{\mathrm{c}e} : (\boldsymbol{\sigma} - p_e \mathbf{1}) \,\mathrm{d}\Omega + \int_{\Gamma_e} \mathbf{v}'_e (\boldsymbol{\sigma} - p_e \mathbf{1}) \cdot \mathbf{n}_e \,\mathrm{d}\Gamma = 0, \quad e = 1, \ldots, \mathrm{NEL}. \tag{42b}$$

Since $\mathbf{n}_e$ is constant within each element, we obtain from Eq. (42a)

$$\tilde{\boldsymbol{\varepsilon}}'_{\mathrm{c}e} = -\frac{1}{l_e} (\mathbf{v}'_e \otimes \mathbf{n}_e)^{\mathrm{sym}} \quad \text{with } l_e = \frac{A_e}{L_e}, \quad A_e = m(\Omega_e), \;\; L_e = m(\Gamma_e). \tag{43}$$

Hence, Eq. (42b) becomes

$$\mathbf{v}'_e \cdot \left[-\frac{1}{l_e} \int_{\Omega_e} (\boldsymbol{\sigma} - p_e \mathbf{1}) \cdot \mathbf{n}_e \,\mathrm{d}\Omega + \int_{\Gamma_e} (\boldsymbol{\sigma} - p_e \mathbf{1}) \cdot \mathbf{n}_e \,\mathrm{d}\Gamma \right] = 0, \quad e = 1, \ldots, \mathrm{NEL}. \tag{44}$$

5.1.2. Mass conservation

Quantities related to enhanced pressure and pressure gradient are chosen piecewise constant within each Ω_e such that

$$\begin{aligned} \gamma &= \sum_{e=1}^{\mathrm{NEL}} \chi_e \gamma_e, \qquad \tilde{p}_{\mathrm{c}} = \sum_{e=1}^{\mathrm{NEL}} \chi_e \tilde{p}_{\mathrm{c}e}, \qquad q = \sum_{e=1}^{\mathrm{NEL}} \chi_e q_e, \\ \tilde{\boldsymbol{\eta}}_{\mathrm{c}} &= \sum_{e=1}^{\mathrm{NEL}} \chi_e \tilde{\boldsymbol{\eta}}_{\mathrm{c}e}, \qquad \mathbf{w} = \sum_{e=1}^{\mathrm{NEL}} \chi_e \mathbf{w}_e. \end{aligned} \tag{45}$$

Upon inserting these FE approximations into Eqs. (36b), (36c) and (38b), we obtain

$$\int_{\Omega_e} \gamma'_e \tilde{p}'_e \,\mathrm{d}\Omega = \int_{\Omega_e} \gamma'_e \tilde{p}'_{\mathrm{c}e} \,\mathrm{d}\Omega + \int_{\Gamma_e} \gamma'_e q'_e \,\mathrm{d}\Gamma = 0, \quad e = 1, \ldots, \mathrm{NEL}, \tag{46}$$

$$\begin{aligned} \int_{\Omega_e} \mathbf{w}'_e \cdot \tilde{\boldsymbol{\eta}}'_e \,\mathrm{d}\Omega &= \int_{\Omega_e} \mathbf{w}'_e \cdot \tilde{\boldsymbol{\eta}}'_{\mathrm{c}e} \,\mathrm{d}\Omega + \int_{\Omega_e} \mathbf{w}_e \cdot \nabla(\delta_\Gamma q'_e) \,\mathrm{d}\Omega \\ &= \int_{\Omega_e} \mathbf{w}'_e \cdot \tilde{\boldsymbol{\eta}}'_{\mathrm{c}e} \,\mathrm{d}\Omega - \int_{\Gamma_e} \nabla \cdot \mathbf{w}'_e q'_e \,\mathrm{d}\Gamma + \int_{\partial\Omega_e} \mathbf{w}'_e \cdot \delta_\Gamma q'_e \bar{\mathbf{n}}_e \,\mathrm{d}\Gamma = 0, \end{aligned} \tag{47}$$

$$\int_{\Omega_e} \tilde{\boldsymbol{\eta}}'_e \cdot \mathbf{v}_\mathrm{d}\,\mathrm{d}\Omega - \int_{\Omega_e} \tilde{p}'_e \dot{\varepsilon}_{\mathrm{v}e}\,\mathrm{d}\Omega = \int_{\Omega_e} \tilde{\boldsymbol{\eta}}'_{\mathrm{c}e} \cdot \mathbf{v}_\mathrm{d}\,\mathrm{d}\Omega - \int_{\Gamma_e} q'_e \nabla \cdot \mathbf{v}_\mathrm{d}\,\mathrm{d}\Gamma + \int_{\partial\Omega_e} \delta_\Gamma q'_e \bar{\mathbf{n}}_e \cdot \mathbf{v}_\mathrm{d}\,\mathrm{d}\Gamma - \int_{\Omega_e} \tilde{p}'_{\mathrm{c}e} \dot{\varepsilon}_{\mathrm{v}e}\,\mathrm{d}\Omega - \int_{\Gamma_e} q'_e \dot{\varepsilon}\,\mathrm{d}\Gamma = 0, \tag{48}$$

where $\bar{\mathbf{n}}_e$ is the outward unit normal vector of the element boundary. Since $\tilde{p}_{\mathrm{c}e}$, q_e and $\mathbf{w}_e$ are elementwise constant fields, we obtain from Eqs. (46) and (47), the relations,

$$\tilde{p}'_{\mathrm{c}e} = -\frac{1}{l_e} q'_e, \qquad \tilde{\boldsymbol{\eta}}'_{\mathrm{c}e} = -\frac{1}{A_e} \bar{\mathbf{n}}_{\partial\Gamma} q'_e, \tag{49}$$

where $\bar{\mathbf{n}}_{\partial\Gamma} = \bar{\mathbf{n}}_e(\partial_1\Gamma_e) + \bar{\mathbf{n}}_e(\partial_2\Gamma_e)$, i.e., the sum of unit normal vectors of the element boundary at the end points of the element-embedded line. Hence, Eq. (48) becomes

$$q'_e \left[\frac{1}{l_e} \int_{\Omega_e} \dot{\varepsilon}_{\mathrm{v}e}\,\mathrm{d}\Omega - \int_{\Gamma_e} \dot{\varepsilon}_{\mathrm{v}e}\,\mathrm{d}\Gamma - \int_{\Gamma_e} \nabla \cdot \mathbf{v}_\mathrm{d}\,\mathrm{d}\Gamma - \frac{1}{A_e} \int_{\Omega_e} \bar{\mathbf{n}}_{\partial\Gamma} \cdot \mathbf{v}_\mathrm{d}\,\mathrm{d}\Omega + \bar{\mathbf{n}}_{\partial\Gamma} \cdot \mathbf{v}_\mathrm{d} \right] = 0 \quad \text{for } e = 1, \ldots, \mathrm{NEL}. \tag{50}$$

5.1.3. Regularization of singular fields

In contrast to the variational fields, the actual enhanced fields are chosen to have the regularized form in accordance with the development of the regularized strong discontinuities for the continuum in Section 3.1. In view of Eqs. (33) and (49), we thus consider element approximation in terms of compatible and regularized enhanced fields such that

$$\boldsymbol{\varepsilon}_e = \boldsymbol{\varepsilon}_{\mathrm{c}e} + \frac{1}{\delta}\left(f - \frac{\delta}{l_e}\right)(\mathbf{n}_e \otimes [\![\mathbf{u}]\!]_e)^{\mathrm{sym}} \quad \Rightarrow \quad \dot{\varepsilon}_{\mathrm{v}e} = \dot{\varepsilon}_{\mathrm{vc}e} + \frac{1}{\delta}\left(f - \frac{\delta}{l_e}\right)\mathbf{n}_e \cdot [\![\dot{\mathbf{u}}]\!]_e, \tag{51a}$$

$$p_e = p_{\mathrm{c}e} + \left(f - \frac{\delta}{l_e}\right)[\![p]\!]_e, \tag{51b}$$

$$\mathbf{v}_\mathrm{d} = -k\left(\nabla p_{\mathrm{c}e} + \frac{g}{\delta}\mathbf{n}_e [\![p]\!]_e\right) = \mathbf{v}_{\mathrm{d,c}} + g[\![\mathbf{v}_\mathrm{d}]\!] \quad \text{with } [\![\mathbf{v}_\mathrm{d}]\!] = -\frac{k}{\delta}[\![p]\!]_e \mathbf{n}_e, \tag{51c}$$

$$\nabla \cdot \mathbf{v}_\mathrm{d} = -k\left(\nabla \cdot \nabla p_{\mathrm{c}e} + \frac{h}{\delta^2}[\![p]\!]_e\right) = \nabla \cdot \mathbf{v}_{\mathrm{d,c}} + \frac{h}{\delta}\mathbf{n}_e \cdot [\![\mathbf{v}_\mathrm{d}]\!], \tag{51d}$$

where $[\![\mathbf{u}]\!]_e$, $[\![p]\!]_e$ are the displacement discontinuity and pressure discontinuity parameters of the element, respectively. Moreover, $f(n)$, $g(n)$ and $h(n)$ are the regularization functions given in Fig. 2. We note that, given the regularized strain, the stress rate response of the element can be derived in complete analogy with the continuum situation in Eq. (17).

Up to this point, the formulation is general in terms of dimension of the problem and choice of displacement/pressure-based base element. However, in the subsequent developments, we explicitly introduce properties of the chosen element, (Fig. 3). We note in particular, from Eq. (51c) and (51d), that $\mathbf{v}_{\mathrm{d,c}}$ is constant whereby $\nabla \cdot \mathbf{v}_{\mathrm{d,c}} = 0$. In view of Eqs. (51c) and (13), this leads to that the two last terms in Eq. (50) are identical and will thus vanish from this equation. Hence, we consider Eq. (50) restated as

$$q'_e \left[\frac{1}{l_e} \int_{\Omega_e} \dot{\varepsilon}_{\mathrm{v}e}\,\mathrm{d}\Omega - \int_{\Gamma_e} \dot{\varepsilon}_{\mathrm{v}e}\,\mathrm{d}\Gamma - \int_{\Gamma_e} \frac{h}{\delta}\mathbf{n}_e \cdot [\![\mathbf{v}_\mathrm{d}]\!]\,\mathrm{d}\Gamma \right] = 0, \quad e = 1, \ldots, \mathrm{NEL}. \tag{52}$$

5.2. Finite element equations

Upon inserting the preceding FE discretizations into Eqs. (37a), (38a), (44) and (50), we obtain the discretized formulation:

$$\overset{\text{NEL}}{\underset{e=1}{\mathbf{A}}}\left[\mathbf{b}_e - \mathbf{f}^{\text{ext}}_{\text{u}e}\right] = \mathbf{0}, \tag{53a}$$

$$\overset{\text{NEL}}{\underset{e=1}{\mathbf{A}}}\left[\mathbf{c}_e - \mathbf{f}^{\text{ext}}_{\text{p}e}\right] = \mathbf{0}, \tag{53b}$$

$$\mathbf{r}_e = \mathbf{0}, \quad e = 1, \ldots, \text{NEL}, \tag{53c}$$

$$s_e = 0, \quad e = 1, \ldots, \text{NEL}, \tag{53d}$$

where Eqs. (53a) and (53b) are the global momentum and mass balance and Eqs. (53c) and (53d) are solved locally and represents momentum and mass balance across the element-embedded band. Subsequently, we introduce the backward Euler method for the temporal integration. The internal node forces and local traction/mass balance are given by

$$\begin{aligned}
\mathbf{b}_e &= \overset{6}{\underset{I=1}{\mathbf{A}_{\text{u}}}} \int_{\Omega_e} (\boldsymbol{\sigma} - p_e\mathbf{1}) \cdot \mathbf{m}^I_{\text{u}}\, \text{d}\Omega, \\
\mathbf{c}_e &= \overset{3}{\underset{I=1}{\mathbf{A}_{\text{p}}}} \int_{\Omega_e} (\Delta t \mathbf{m}^I_{\text{p}} \cdot \mathbf{v}_{\text{d}} - \boldsymbol{N}^I_{\text{p}} \Delta\varepsilon_{\text{v}e})\, \text{d}\Omega, \\
\mathbf{r}_e &= \int_{\Gamma_e} (\boldsymbol{\sigma} - p_e\mathbf{1}) \cdot \mathbf{n}\, \text{d}\Gamma - \frac{1}{l_e}\int_{\Omega_e} (\boldsymbol{\sigma} - p_e\mathbf{1})\mathbf{n}\, \text{d}\Omega, \\
s_e &= \int_{\Gamma_e} \Delta\varepsilon_{\text{v}e}\, \text{d}\Gamma - \frac{1}{l_e}\int_{\Omega_e} \Delta\varepsilon_{\text{v}e}\, \text{d}\Omega - \Delta t \int_{\Gamma_e} \frac{4}{\delta}[\![\mathbf{v}_{\text{d}}]\!] \cdot \mathbf{n}\, \text{d}\Gamma,
\end{aligned} \tag{54}$$

whereas the external node forces are defined as

$$\begin{aligned}
\mathbf{f}^{\text{ext}}_{\text{u}e} &= \overset{6}{\underset{I=1}{\mathbf{A}_{\text{u}}}} \int_{\Omega_e} N^I_{\text{u}} \hat{\rho}\mathbf{b}\, \text{d}\Omega + \overset{6}{\underset{I=1}{\mathbf{A}_{\text{u}}}} \int_{\Gamma_e} N^I_{\text{u}} \bar{\mathbf{t}}\, \text{d}\Gamma, \\
\mathbf{f}^{\text{ext}}_{\text{p}e} &= \overset{3}{\underset{I=1}{\mathbf{A}_{\text{p}}}} \int_{\Omega_e} \Delta t N^I_{\text{p}} \bar{q}\, \text{d}\Omega.
\end{aligned} \tag{55}$$

In Eqs. (53a) and (54), we introduced the assembly operators $\mathbf{A}$, $\mathbf{A}_{\text{u}}$ and $\mathbf{A}_{\text{p}}$. The operator $\mathbf{A}$ determine the position in the global FE vector, where the element contribution fits are based on the global nodal-element topology. The element internal operators, e.g., $\mathbf{A}_{\text{u}}$ on the other hand, determines the position of each local contribution within the element vector from the local node topology, i.e., $\mathbf{A}_{\text{u}}$ defines the identity,

$$\sum_{I=1}^{\text{NOEL}} (\mathbf{m}^I_{\text{u}} \otimes \mathbf{u}^I_e)^{\text{sym}} : \boldsymbol{\sigma} \equiv \hat{\mathbf{u}}^t_e \left[\overset{\text{NOEL}}{\underset{I=1}{\mathbf{A}_{\text{u}}}} \mathbf{m}^I_{\text{u}} \cdot \boldsymbol{\sigma} \right], \tag{56}$$

where the vector $\hat{\mathbf{u}}_e$ contains the element-nodal displacement variables. Likewise, the vector $\hat{\mathbf{p}}_e$ contains the element-nodal pressure variables.

5.3. Solution procedure

5.3.1. Tangent relation

The non-linear equations (53) are conveniently solved using Newton–Raphson method, whereby the proper linearization of Eq. (54) is required. For this purpose, we first note that

$$\mathrm{d}\mathbf{b}_e = \overset{6}{\underset{I=1}{\mathbf{A}}}{}_{\mathrm{u}} \int_{\Omega_e} (\mathrm{d}\boldsymbol{\sigma} - \mathrm{d}p_e\mathbf{1}) \cdot \mathbf{m}_{\mathrm{u}}^I \,\mathrm{d}\Omega, \tag{57a}$$

$$\mathrm{d}\mathbf{c}_e = \overset{3}{\underset{I=1}{\mathbf{A}}}{}_{\mathrm{p}} \int_{\Omega_e} (\Delta t \mathbf{m}_{\mathrm{p}}^I \cdot \mathrm{d}\mathbf{v}_{\mathrm{d}} - N_{\mathrm{p}}^I \,\mathrm{d}\varepsilon_{ve}) \,\mathrm{d}\Omega, \tag{57b}$$

$$\mathrm{d}\mathbf{r}_e = \int_{\Gamma_e} (\mathrm{d}\boldsymbol{\sigma} - \mathrm{d}p_e\mathbf{1}) \cdot \mathbf{n}_e \,\mathrm{d}\Gamma - \frac{1}{l_e} \int_{\Omega_e} (\mathrm{d}\boldsymbol{\sigma} - \mathrm{d}p_e\mathbf{1}) \cdot \mathbf{n}_e \,\mathrm{d}\Omega, \tag{57c}$$

$$\mathrm{d}s_e = \int_{\Gamma_e} \mathrm{d}\varepsilon_{ve} \,\mathrm{d}\Gamma - \frac{1}{l_e} \int_{\Omega_e} \mathrm{d}\varepsilon_{ve} \,\mathrm{d}\Gamma - \Delta t \int_{\Gamma_e} \frac{4}{\delta} \mathrm{d}[\![\mathbf{v}_{\mathrm{d}}]\!] \cdot \mathbf{n}_e \,\mathrm{d}\Gamma, \tag{57d}$$

where

$$\mathrm{d}\boldsymbol{\sigma} = \left[\overset{6}{\underset{I=1}{\mathbf{A}}}{}_{\mathrm{u}} \mathbf{E} \cdot \mathbf{m}_{\mathrm{u}}^I \right] \mathrm{d}\hat{\mathbf{u}}_e + \frac{1}{\delta} \left(f - \frac{\delta}{l_e} \right) \mathbf{n}_e \cdot \mathbf{E} \cdot \mathrm{d}[\![\mathbf{u}]\!]_e, \tag{58a}$$

$$\mathrm{d}p_e = \left[\overset{3}{\underset{I=1}{\mathbf{A}}}{}_{\mathrm{p}} N_{\mathrm{p}}^I \right] \mathrm{d}\hat{\mathbf{p}}_e + \left(f - \frac{\delta}{l_e} \right) \mathrm{d}[\![p]\!]_e, \tag{58b}$$

$$\mathrm{d}\varepsilon_{ve} = \left[\overset{6}{\underset{I=1}{\mathbf{A}}}{}_{\mathrm{u}} \mathbf{m}_{\mathrm{u}}^I \right] \mathrm{d}\hat{\mathbf{u}}_e + \frac{1}{\delta} \left(f - \frac{\delta}{l_e} \right) \mathbf{n}_e \cdot \mathrm{d}[\![\mathbf{u}]\!]_e, \tag{58c}$$

$$\mathrm{d}\mathbf{v}_{\mathrm{d}} = -\left[\overset{3}{\underset{I=1}{\mathbf{A}}}{}_{\mathrm{p}} k \mathbf{m}_{\mathrm{p}}^I \right] \mathrm{d}\hat{\mathbf{p}}_e + g \,\mathrm{d}[\![\mathbf{v}_{\mathrm{d}}]\!], \tag{58d}$$

$$\mathrm{d}[\![\mathbf{v}_{\mathrm{d}}]\!] = -\frac{k}{\delta} \mathbf{n}_e \,\mathrm{d}[\![p]\!]_e. \tag{58e}$$

In view of Eqs. (57) and (58), the element tangent stiffness formally takes the form:

$$\begin{bmatrix} \mathrm{d}\mathbf{b}_e \\ \mathrm{d}\mathbf{c}_e \\ \mathrm{d}\mathbf{r}_e \\ \mathrm{d}s_e \end{bmatrix} = \begin{bmatrix} \mathbf{K}_e^u & \mathbf{C}_e & \mathbf{F}_e & \mathbf{P}_e \\ \mathbf{C}_e' & \mathbf{K}_e^{\mathrm{p}} & \mathbf{G}_e & \mathbf{0} \\ \mathbf{F}_e' & \mathbf{G}_e' & \mathbf{H}_e & \mathbf{S}_e \\ \mathbf{P}_e' & \mathbf{0} & \mathbf{S}_e' & D_e \end{bmatrix} \begin{bmatrix} \mathrm{d}\hat{\mathbf{u}}_e \\ \mathrm{d}\hat{\mathbf{p}}_e \\ \mathrm{d}[\![\mathbf{u}]\!]_e \\ \mathrm{d}[\![p]\!]_e \end{bmatrix}, \tag{59}$$

where it may be noted that the stiffness matrix is unsymmetric due to the difference in the enhanced variational and the enhanced actual fields. In Eq. (59), the various elements are defined as

$$\mathbf{K}_e^u = \overset{6}{\underset{I=1}{\mathbf{A}}}{}_{\mathrm{u}} \overset{6}{\underset{J=1}{\mathbf{A}}}{}_{\mathrm{u}} \int_{\Omega_e} \mathbf{m}_{\mathrm{u}}^I \cdot \mathbf{E} \cdot \mathbf{m}_{\mathrm{u}}^J \mathrm{d}\Omega, \tag{60a}$$

$$\mathbf{K}_e^{\mathrm{p}} = -\overset{3}{\underset{I=1}{\mathbf{A}}}{}_{\mathrm{p}} \overset{3}{\underset{J=1}{\mathbf{A}}}{}_{\mathrm{p}} \int_{\Omega_e} \Delta t k \mathbf{m}_{\mathrm{p}}^I \cdot \mathbf{m}_{\mathrm{p}}^J \,\mathrm{d}\Omega, \tag{60b}$$

$$\mathbf{C}_e = -\mathop{\mathbf{A}}_{I=1}^{6}{}_{\mathrm{u}}\mathop{\mathbf{A}}_{J=1}^{3}{}_{\mathrm{p}}\int_{\Omega_e}\mathbf{m}_{\mathrm{u}}^{I}N_{\mathrm{p}}^{J}\,\mathrm{d}\Omega, \qquad \mathbf{C}'_e = -\mathop{\mathbf{A}}_{I=1}^{3}{}_{\mathrm{p}}\mathop{\mathbf{A}}_{J=1}^{6}{}_{\mathrm{u}}\int_{\Omega_e}N_{\mathrm{p}}^{I}\mathbf{m}_{\mathrm{u}}^{J}\,\mathrm{d}\Omega = \mathbf{C}_e^{T}, \tag{60c}$$

$$\mathbf{H}_e = \int_{\Gamma_e}\left(\frac{1}{\delta}-\frac{1}{l_e}\right)\mathbf{n}_e\cdot\mathbf{E}\cdot\mathbf{n}_e\,\mathrm{d}\Gamma + \int_{\Omega_e}\frac{1}{l_e^2}\mathbf{n}_e\cdot\mathbf{E}\cdot\mathbf{n}_e\,\mathrm{d}\Omega, \tag{60d}$$

$$\mathbf{G}_e = \mathop{\mathbf{A}}_{I=1}^{3}{}_{\mathrm{p}}\int_{\Omega_e}\frac{1}{l_e}N_{\mathrm{p}}^{I}\mathbf{n}_e\,\mathrm{d}\Omega, \qquad \mathbf{G}'_e = \mathop{\mathbf{A}}_{I=1}^{3}{}_{\mathrm{p}}\left[-\int_{\Gamma_e}N_{\mathrm{p}}^{I}\mathbf{n}_e\,\mathrm{d}\Gamma + \int_{\Omega_e}\frac{1}{l_e}N_{\mathrm{p}}^{I}\mathbf{n}_e\,\mathrm{d}\Omega\right], \tag{60e}$$

$$\mathbf{F}_e = -\mathop{\mathbf{A}}_{I=1}^{6}{}_{\mathrm{u}}\int_{\Omega_e}\frac{1}{l_e}\mathbf{m}_{\mathrm{u}}^{I}\cdot\mathbf{E}\cdot\mathbf{n}_e\,\mathrm{d}\Omega, \tag{60f}$$

$$\mathbf{F}'_e = \mathop{\mathbf{A}}_{I=1}^{6}{}_{\mathrm{u}}\left[\int_{\Gamma_e}\mathbf{n}_e\cdot\mathbf{E}\cdot\mathbf{m}_{\mathrm{u}}^{I}\,\mathrm{d}\Gamma - \int_{\Omega_e}\frac{1}{l_e}\mathbf{n}_e\cdot\mathbf{E}\cdot\mathbf{m}_{\mathrm{u}}^{I}\,\mathrm{d}\Omega\right], \tag{60g}$$

$$D_e = \int_{\Gamma_e}\Delta t\frac{4k}{\delta^2}\mathrm{d}\Gamma, \tag{60h}$$

$$\mathbf{S}_e = -\int_{\Gamma_e}\mathbf{n}_e\,\mathrm{d}\Gamma, \qquad \mathbf{S}'_e = \int_{\Gamma_e}\frac{1}{\delta}\mathbf{n}_e\,\mathrm{d}\Gamma, \tag{60i}$$

$$\mathbf{P}_e = \mathop{\mathbf{A}}_{I=1}^{6}{}_{\mathrm{u}}\int_{\Omega_e}\frac{\delta}{l_e}\mathbf{m}_{\mathrm{u}}^{I}\,\mathrm{d}\Omega, \qquad \mathbf{P}'_e = \mathop{\mathbf{A}}_{I=1}^{6}{}_{\mathrm{u}}\left[\int_{\Gamma_e}\mathbf{m}_{\mathrm{u}}^{I}\,\mathrm{d}\Gamma - \int_{\Omega_e}\frac{1}{l_e}\mathbf{m}_{\mathrm{u}}^{I}\,\mathrm{d}\Omega\right]. \tag{60j}$$

5.3.2. Overall solution algorithm (global problem)

In the actual FE computations, displacement and pressure discontinuities are condensed at element level by partial inversion of Eq. (59) such that the resulting set of equations contains only displacement and pressure variables of the "base" element approximation. Moreover, as compared to a standard partial inversion of the local element problems, we adopt a slightly different procedure where the local equations are solved completely for each global iterate. The procedure is similar to that in Simo et al. (1993a) and may be outlined as follows: the improved incremental nodal solution for time $t = t_{n+1}$ is obtained from

$$\begin{bmatrix}\Delta\hat{\mathbf{u}}_e^{i+1}\\ \Delta\hat{\mathbf{p}}_e^{i+1}\end{bmatrix} = \begin{bmatrix}\Delta\hat{\mathbf{u}}_e^{i}\\ \Delta\hat{\mathbf{p}}_e^{i}\end{bmatrix} + \boldsymbol{\xi}_e, \quad e = 1,\ldots,\mathrm{NEL}, \tag{61}$$

where the iterative improvement $\boldsymbol{\xi}_e$ is evaluated as

(1) solve $(\llbracket\mathbf{u}\rrbracket_e^{(i)}, \llbracket p\rrbracket_e^{(i)})$ from

$$\begin{cases}\mathbf{r}_e^{(i)} = \mathbf{0},\\ s_e^{(i)} = 0,\end{cases} \quad e = 1,\ldots,\mathrm{NEL}, \tag{62a}$$

(2) then solve $\boldsymbol{\xi}_e$ from

$$\mathop{\mathbf{A}}_{e=1}^{\mathrm{NEL}}\left[\hat{\mathbf{K}}_e\boldsymbol{\xi}_e + \mathbf{g}_e^{(i)}\right] = \mathbf{0}, \tag{62b}$$

where $\hat{\mathbf{K}}_e$ is the partly inverted element stiffness and $\mathbf{g}_e^{(i)}$ is the out-of-balance force with respect to the global equations, defined as

$$\hat{\mathbf{K}}_e = \begin{bmatrix} \mathbf{K}_e^u & \mathbf{C}_e \\ \mathbf{C}_e' & \mathbf{K}_e^{\mathrm{p}} \end{bmatrix} - \begin{bmatrix} \mathbf{F}_e & \mathbf{P}_e \\ \mathbf{G}_e & \mathbf{0} \end{bmatrix} \begin{bmatrix} \mathbf{H}_e & \mathbf{S}_e \\ \mathbf{S}_e' & \mathbf{D}_e \end{bmatrix}^{-1} \begin{bmatrix} \mathbf{F}_e' & \mathbf{G}_e' \\ \mathbf{P}_e' & \mathbf{0} \end{bmatrix}, \qquad \mathbf{g}_e^{(i)} = \begin{bmatrix} \mathbf{b}_e^{(i)} \\ \mathbf{c}_e^{(i)} \end{bmatrix} - \begin{bmatrix} \mathbf{f}_{\mathrm{u}e}^{\mathrm{ext}} \\ \mathbf{f}_{\mathrm{p}e}^{\mathrm{ext}} \end{bmatrix}. \tag{63a, b}$$

In Eq. (63b) the external action is the one evaluated at time $t = t_{n+1}$. We emphasize that in the algorithm given in Eqs. (61) and (62), the local element problems are solved with fixed node quantities.

5.3.3. Discrete version of condition for onset of localization

Let us assess the condition for onset of localization for the discretized problem. Given equilibrated nodal variables $\hat{\mathbf{u}}_e$ and $\hat{\mathbf{p}}_e$ at time $t = t_{n+1}$ from the algorithm in Eqs. (61) and (62), the tangent relation for the local problem becomes

$$\begin{bmatrix} \mathrm{d}\mathbf{r}_e \\ \mathrm{d}s_e \end{bmatrix} = \begin{bmatrix} \mathbf{H}_e & \mathbf{S}_e \\ \mathbf{S}_e' & \mathbf{D}_e \end{bmatrix} \begin{bmatrix} \mathrm{d}[\![\mathbf{u}]\!]_e \\ \mathrm{d}[\![p]\!]_e \end{bmatrix}, \tag{64}$$

In the situation of onset of localization, the state is continuous within each element, and assuming that the tangent stiffness is constant within an element, it is possible to evaluate the integrals in the expression for the tangent matrix in Eq. (64) such that

$$\begin{aligned} \mathrm{d}\mathbf{r}_e &= \frac{L_e}{\delta}\mathbf{Q}_\Gamma \cdot \mathrm{d}[\![\mathbf{u}]\!]_e - L_e \mathbf{n}\, \mathrm{d}[\![p]\!]_e = 0, \\ \mathrm{d}s_e &= \frac{L_e}{\delta}\mathbf{n} \cdot \mathrm{d}[\![\mathbf{u}]\!]_e - 4\Delta t \frac{L_e}{\delta}\mathbf{n} \cdot \mathrm{d}[\![\mathbf{v}_{\mathrm{d}}]\!]_e = 0. \end{aligned} \tag{65}$$

This is the discretized version of the condition for the onset of localization for the continuum mixture Eq. (26). Obviously, the condition for localization in the discretized problem coincides with the continuum situation if the ATS tensor is replaced with the CTS tensor. In fact, in Larsson and Larsson (1999) the sensitivity to the temporal discretization was studied for an undrained porous medium. It appears that onset of localization for the integrated response occurs prematurely as compared to the corresponding predictions of the rate response.

5.3.4. Element solution algorithm (local problems)

As alluded to in Eqs. (61) and (62a,b), we resort to a staggered solution procedure where the local problems are solved completely for every global iteration. The reason for this is to maintain control of the loading situation within an element. In the standard coupled procedure, the element condition will not be satisfied until global equilibrium is reached. This means that a certain loading situation must be assumed a priori (at the beginning of each time step) and the validity of the assumption cannot be checked until the time step is solved. The algorithm to solve the element problems (62a) is based on loading scenarios that can appear within the element (Larsson and Larsson, 1999).

The algorithm for solving the element problem is briefly summarized as follows: as long as an element is elastic, it is identical to the base continuum element. When plastic loading is first detected, we first solve for a discontinuous solution assuming plastic loading within the embedded line and elastic loading in the most stressed integration point belonging to the area integral. When this solution is reached, the validity of the assumption is checked by determining if the state is admissible. If this is the case, the solution is accepted and we may proceed to the next element. If this is not the case, the element problem is solved once again, now allowing plastic loading in all integration points. We note that this algorithm does not make use of the localization condition (26). The reason for this is that even if a singularity of the acoustic tensor is detected in an integration point, it does not always follow that a localized solution within the element is possible. Hence, it appears that an algorithm like the one described above is needed anyway.

The element-embedded line is positioned by the condition that it goes through the integration point of the base element where the trial yield function takes the largest positive value. The direction of the em-

bedded line is then evaluated by means of a bifurcation analysis of the constitutive model for the effective material using the latest converged effective stress, compare discussion in Section 3.2. Once localization has occurred in an element, the line is held fixed throughout the analysis. Since the orientation of the embedded line is unknown prior to the analysis, we do not know at this stage the state history in the integration points of the line integral. Thus, we must somehow determine the state for the previous time station in the new integration points. In the present algorithm, the state for the last time station is evaluated with use of total deformation theory. Another possibility would be to use linear interpolation from the integration points of the area integral.

6. Representative examples

6.1. Preliminaries

In the subsequent examples, a generalized Mohr–Coulomb model with the options of non-associated plastic flow and cohesive, isotropic hardening/softening is used to describe the solid phase response. The yield criterion and plastic flow potential are given as

$$\begin{aligned} &\varphi(\boldsymbol{\sigma}) = a_1\sigma_1 + a_2\sigma_2 + a_3\sigma_3 - K \leqslant 0 \ \text{ with } \ \sigma_1 \geqslant \sigma_2 \geqslant \sigma_3 \ \text{ and } \ K = 2c\cos\Phi, \\ &\varphi^*(\boldsymbol{\sigma}) = a_1^*\sigma_1 + a_2^*\sigma_2 + a_3^*\sigma_3, \end{aligned} \tag{66}$$

where σ_i are the principal effective stress components and

$$\begin{aligned} &a_1 = 1 + \frac{2-\alpha}{2+\alpha}\sin\Phi, \qquad a_2 = 1 + \frac{2\alpha}{2+\alpha}\sin\Phi, \qquad a_3 = -1 + \sin\Phi, \\ &a_i^* = a_i + \frac{1}{3}(\beta^* - 1)a_{\text{vol}}, \qquad \beta^* = \frac{\sin\Phi^*}{\sin\Phi}, \qquad a_{\text{vol}} = a_1 + a_2 + a_3. \end{aligned} \tag{67}$$

Here, c is the cohesion, Φ is the angle of internal friction and Φ^* the dilatancy angle. The parameter $0 \leqslant \alpha \leqslant 1$ govern the shape of the yield criterion and plastic potential in the deviator plane and is defined such that $\alpha = 0$ gives the classical Mohr–Coulomb and $\alpha = 1$ the Tresca shape. A detailed description of the model and the consequent consistent linearization is given in Larsson and Runesson (1996b). Hardening/softening is introduced via the cohesion $c = c(\kappa)$. In the numerical simulations, we use for simplicity analytical expressions to determine bifurcation directions where the vertices of the MC-yield surface are not taken into account.

As to the choice of δ, the lower limit of δ is given by the computer precision. The upper limit is given by the condition that it should be small in relation to the characteristic dimension of the boundary value problem. In the subsequent examples, the choice of the shear band width δ is made to fulfill the above requirements and to be in a reasonable order of magnitude of developing shear bands in slope failures. For the effect of varying δ in the numerical results we refer to Larsson and Runesson (1996a).

6.2. Compressed sheet in plane strain – objectivity w.r.t. mesh and element size

As is well known, if one adopt softening to represent a damage process in a standard FE formulation with local rate-independent plasticity, the plastic dissipation strongly depends on the element size. In fact, as the element size tend to zero, the plastic dissipation will also tend to zero, corresponding to infinitely brittle behavior. To study the performance of the proposed element in this respect, we analyze a plane strain sheet with geometry, material and model parameters as given in Fig. 4. To obtain a small stress concentration, a small geometric imperfection is introduced at the upper right point of the sheet (Fig. 4). The material parameters and boundary conditions are chosen to simulate a drained material. This choice is

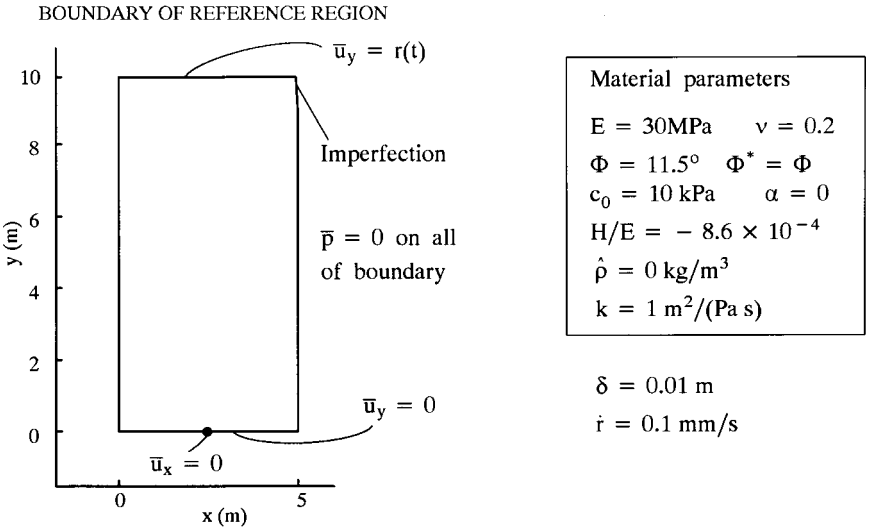

Fig. 4. Geometry, boundary conditions and material parameters for analyzed compressed plane strain sheet. An imperfection is introduced at the upper right point, which is slightly displaced to the left.

made because this is obviously the situation where the mesh sensitivity is most pronounced (Schrefler et al., 1998). Thus, the permeability is set to a very large value and the excess pore pressure is prescribed to zero along the boundary. The analyses are made with three different meshes (Fig. 5).

The load–time/displacement curves (Fig. 6) shows a quite good match between the three meshes. Moreover, the deformation patterns in Fig. 7 and the active localized elements in Fig. 8 shows that the same localization mode is captured for the three meshes. Hence, although not exhibiting complete mesh independence, in view of the obtained results, the formulation appears to behave well in this respect. For comparison, the problem was also analyzed with the same material parameters but with the base element of the present formulation for the finest mesh. We note the inability of the standard element to pick up localization in the present example. This is apparently because the softening modulus is so small relative to the elastic modulus and the size of the elements.

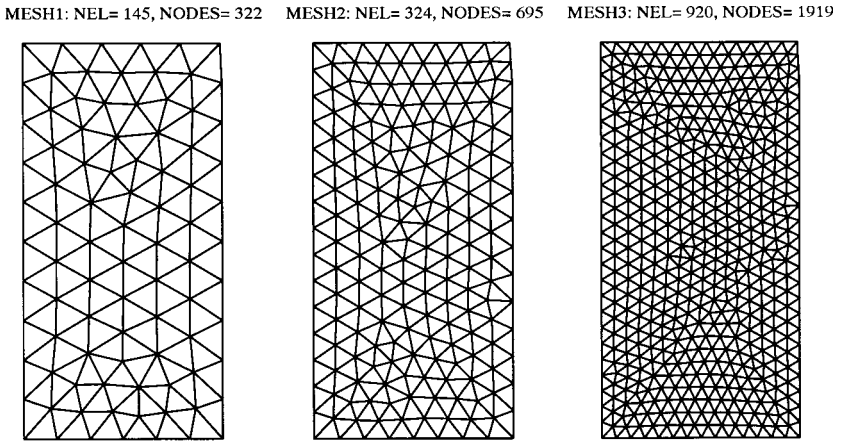

Fig. 5. Different meshes used in simulations of compressed plane strain sheet.

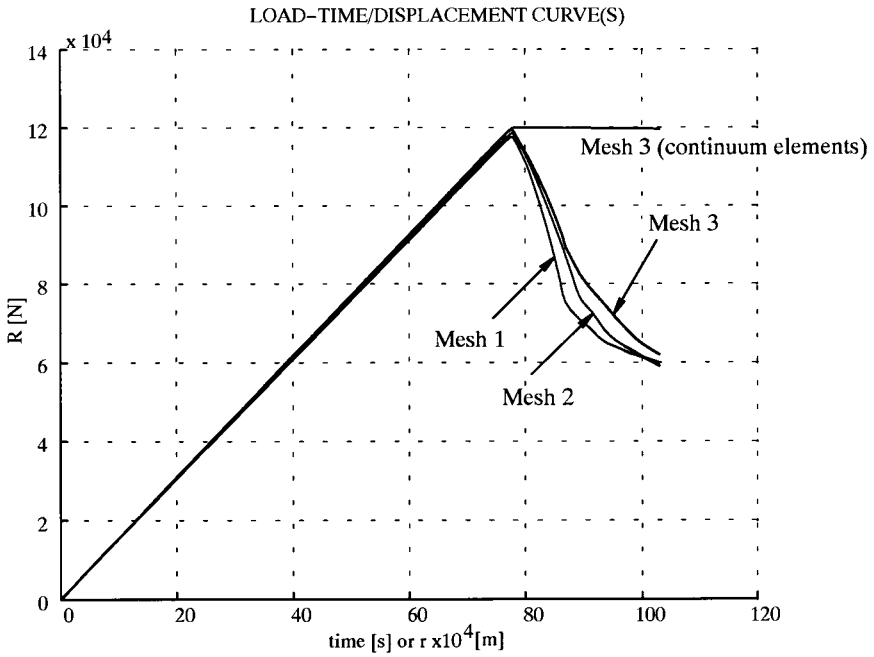

Fig. 6. Load–time/displacement curves obtained with the three different meshes shown in Fig. 5. For comparison also an analysis using the base continuum element with the finest mesh is shown.

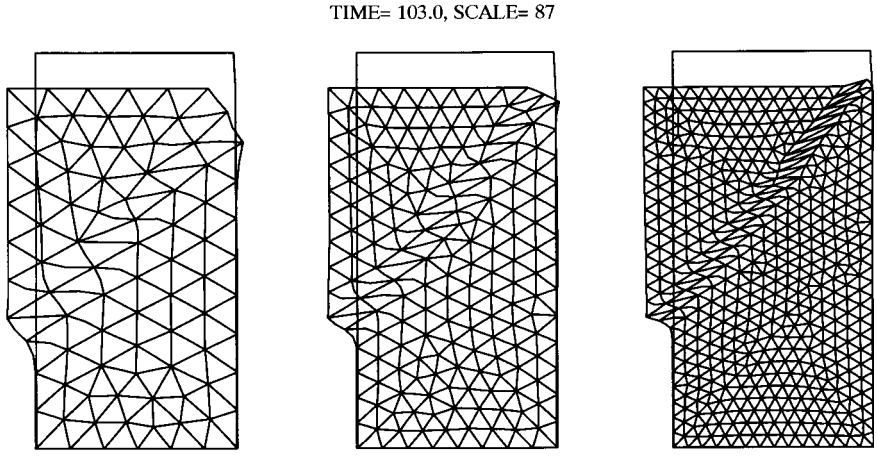

Fig. 7. Deformed meshes of the compressed plane strain sheet at final time step. The undeformed meshes are shown in Fig. 5.

6.3. Slope in plane strain – influence of friction angle on limit load and localization mode

It is of interest to study the significance of the friction angle to the localization properties, such as orientation of the developing shear band and bearing capacity of the structure. To do this, we consider a steep slope with geometry, boundary conditions and material parameters as shown in Fig. 9. Note that the softening behavior is preceded by hardening, corresponding to a ductile material failure. The load is

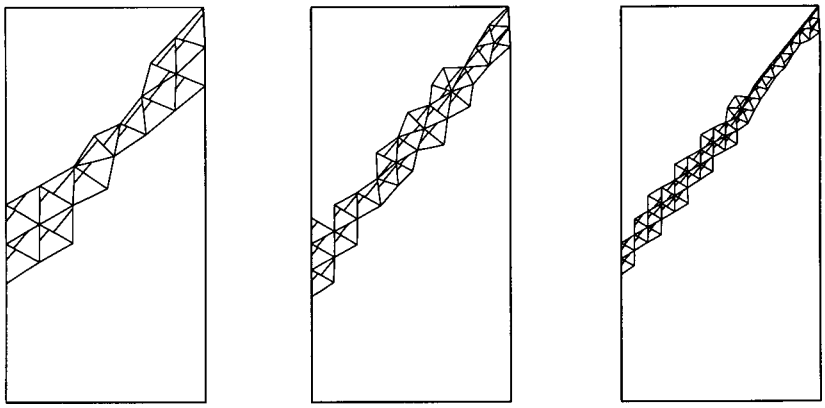

Fig. 8. Currently localized elements at the final time step for the three different meshes given in Fig. 5. The element-embedded lines are also shown.

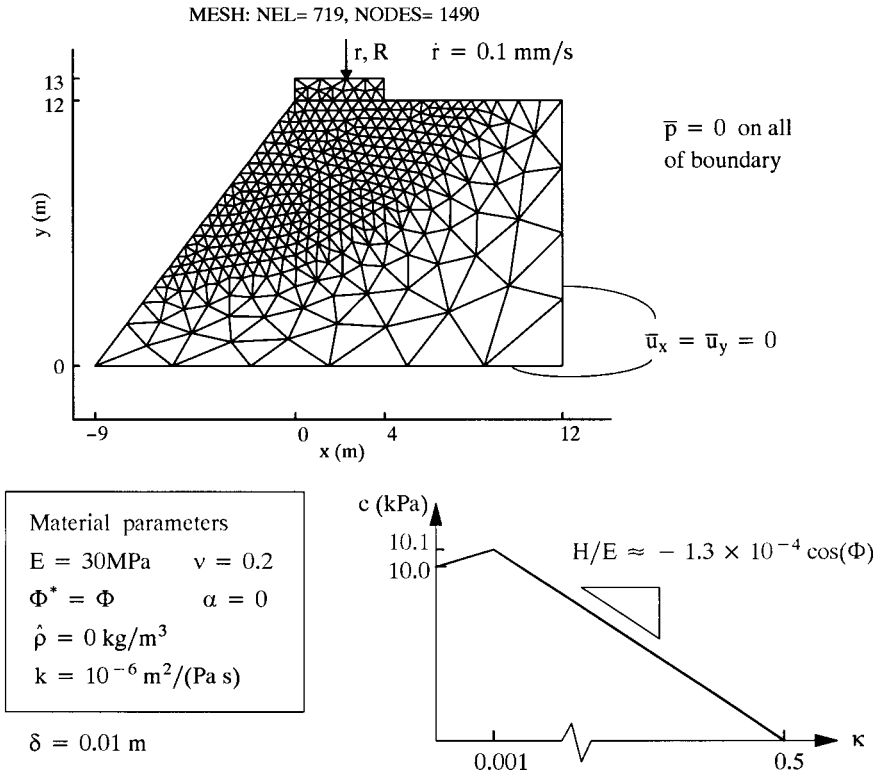

Fig. 9. Geometry, boundary conditions, and material parameters for analyzed steep slopte in plane strain. The slope is analyzed for four different friction angles.

a prescribed vertical displacement of a point on the rigid footing. The position of this point is on the upper surface and 0.3 m to the right from the center of the footing (Fig. 9). For simplicity, the contact between the footing and the soil is assumed to be perfectly rough.

Four simulations are performed with friction angles set to $\Phi = 1.1°, 11.5°, 17.5°, 23.6°$. The deformed meshes that were obtained are shown in Fig. 10. It appears, as expected, that by increased friction angle the "radius" of an inscribed circle segment in the shear band zone increases. For $\Phi = 23.6°$, it appears at first that a localization mode similar to that of a foundation failure develops, but suddenly propagation of the final shear band takes over Fig. 10d. The corresponding load–time/displacement curves are given in Fig. 11. Here, we can see that the limit load increases as the friction angle becomes larger. Moreover, it appears that the structure behaves more brittle at failure for large friction angles.

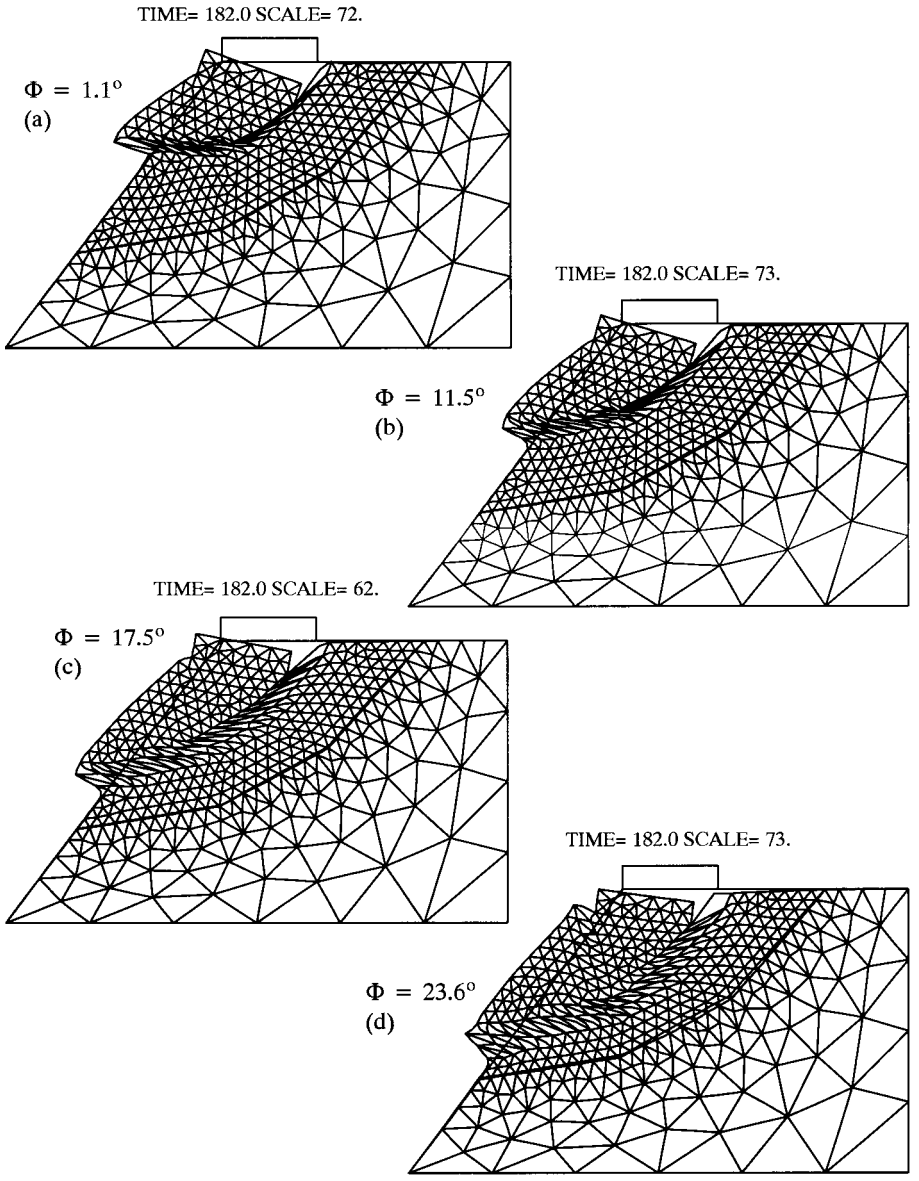

Fig. 10. Deformed meshes obtained with different internal friction angles Φ for the steep slope in Fig. 9.

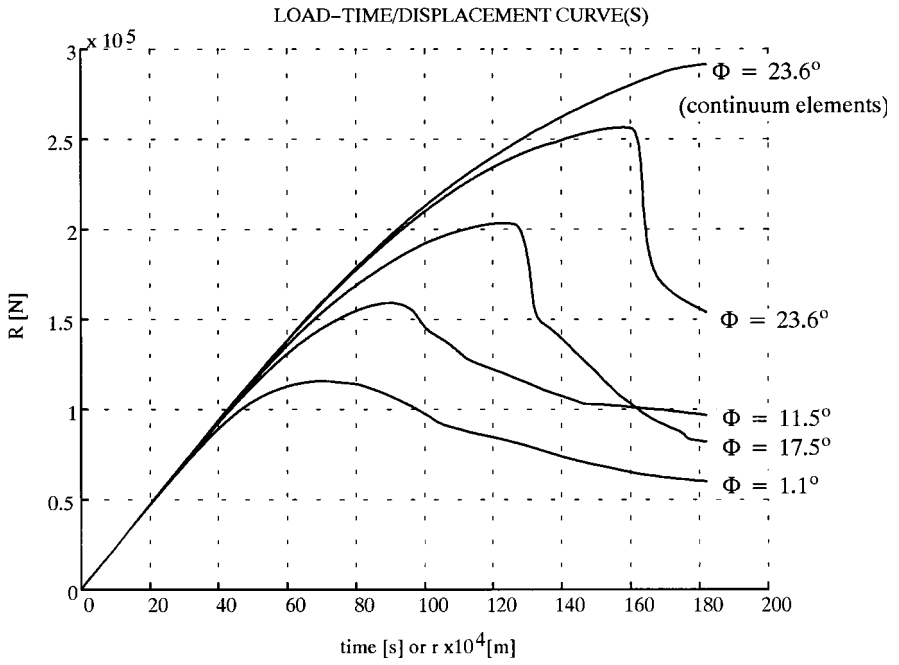

Fig. 11. Load–displacement curves from simulations of the steep slope given in Fig. 9 for various friction angles Φ.

6.4. Slope in plane strain – influence of global drainage conditions on limit load

It is of interest to study the effect of the magnitude of the pore pressure prevailing in the soil mass on the limit load. To this end, the same slope with the same mesh as in the previous example is analyzed. The boundary conditions and material parameters are given in Fig. 12. The boundary conditions for the mass balance is that the boundary is impermeable except where the pressure is prescribed (Fig. 12). Apart from this pressure, the loading consists of a prescribed vertical displacement as in the previous example. The analyses are performed for four different choices of prescribed excess pore pressure: $\bar{p} = 1$ kPa, $\bar{p} = 2$ kPa, $\bar{p} = 4$ kPa and $\bar{p} = 8$ kPa.

From the load–time/displacement curves in Fig. 13, we can see that as the prescribed excess pore pressure is increased the limit load decreases. This is expected because for a given external load, when increasing the excess pore pressure, the effective stress state is forced towards the vertex in the cone of admissible states, thus, losing shear strength. The deformed meshes are not shown here but they are very similar for the different analyses.

6.5. Slope in plane strain – influence of local drainage conditions on limit load and localization mode

To study the influence of local drainage conditions on the localization properties, we reconsider the steep slope analyzed in the two previous examples for various values of the permeability parameter. The slope, with geometry, boundary conditions and material parameters is shown in Fig. 14. The boundary is impermeable and displacements are zero along the lower and right sides.

In view of the load–time/displacement curves in Fig. 15, we obtain an increased and "delayed" peak load in the case of low permeability as compared to the case of high permeability. For comparison, an analysis using the base element is also given. It is noteworthy that using the continuum element gives no limit load in

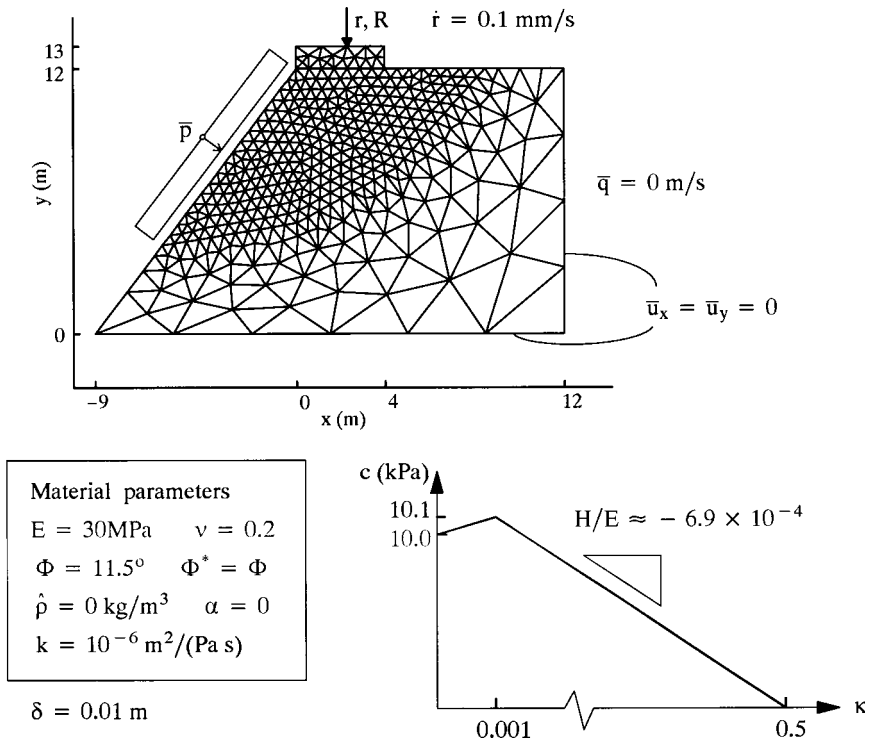

Fig. 12. Geometry, boundary conditions and material parameters for analyzed steep slope in plane strain. The slope is analyzed for different prescribed excess pressures on part of boundary.

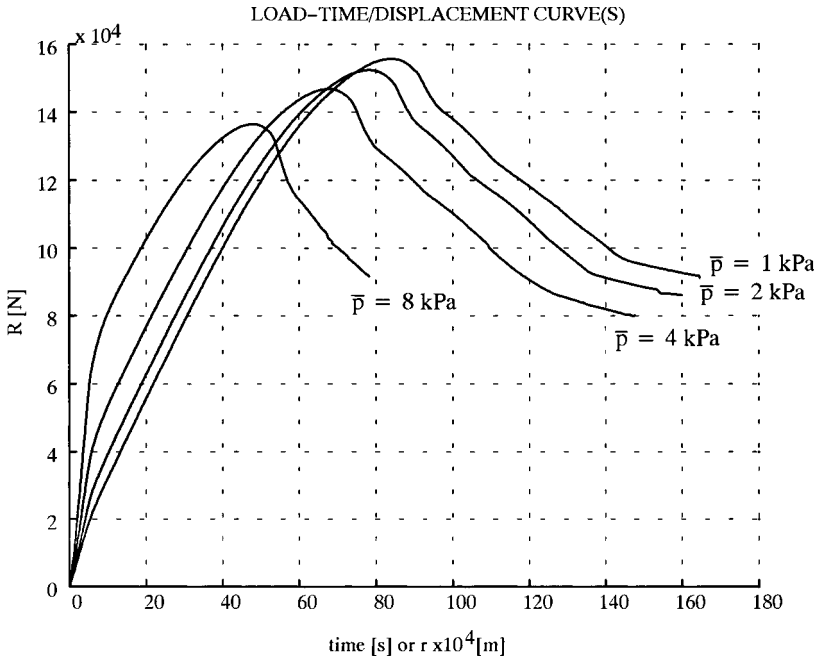

Fig. 13. Load–time/displacement curves from simulations of the steep slope shown in Fig. 12 for different prescribed fluid pressure $\bar{p}$ on part of the boundary. The boundary pressure is applied linearly such that the final value is reached in 5 s.

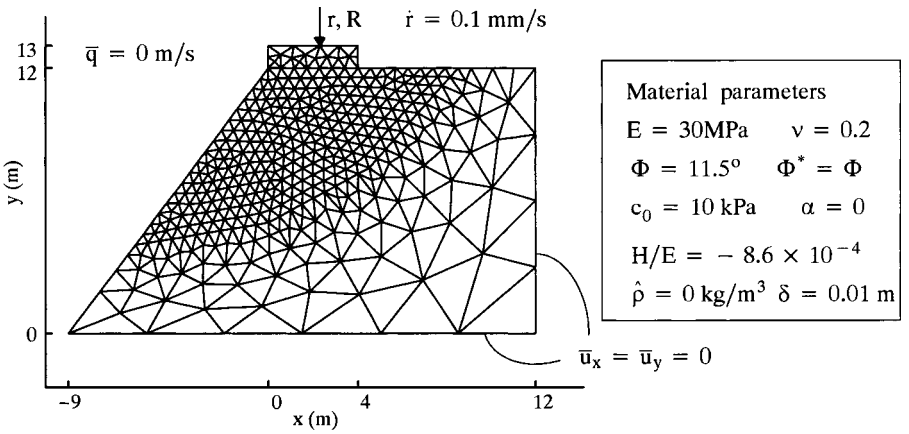

Fig. 14. Geometry, boundary conditions and material parameters for analyzed steep slope in plane strain. The slope is analyzed for various permeabilities.

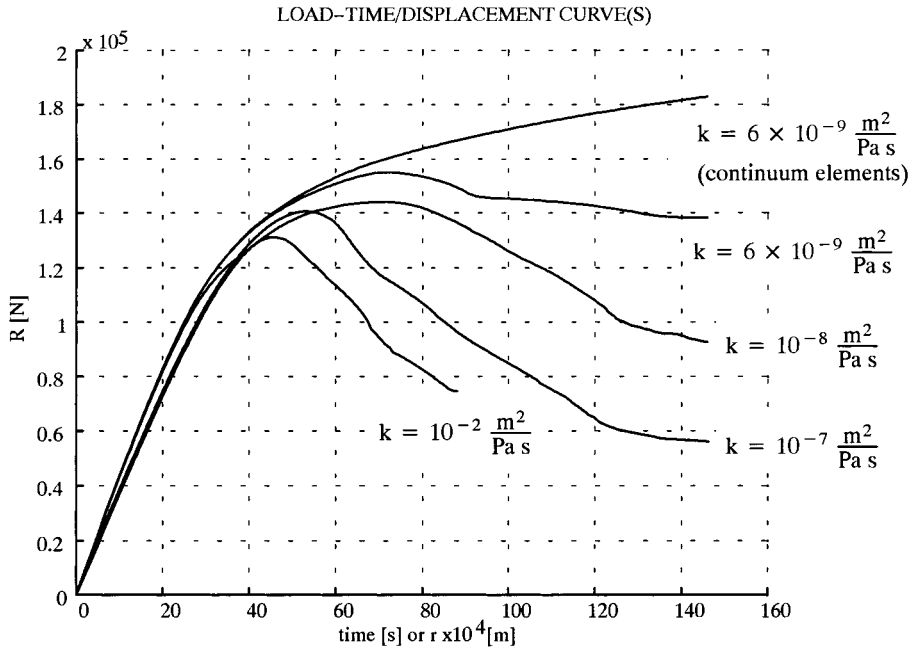

Fig. 15. Load–displacement curves from analyses for various permeabilities.

this case. From the deformed meshes in Fig. 16, we can see that the localization mode is significantly affected by the permeability coefficient. It seems that the tendency is that the radius of inscribed "circle segment" along the shear band tends to be larger as the permeability parameter decreases. We emphasize that the fluid is incompressible, whereby the mixture as a whole also becomes incompressible in the limit as the permeability tends to zero. As a result, our element appears to have limitations in how small magnitude of the permeability we can choose. In the present example, convergence problems were encountered for values smaller than $k = 6 \times 10^{-9}$ m^2/(pa s).

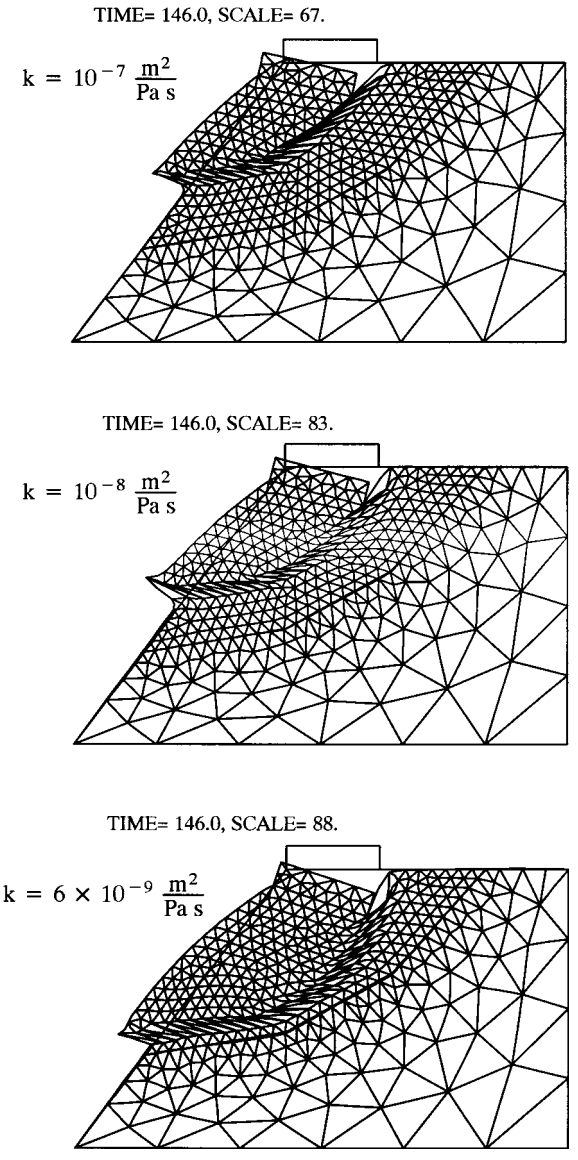

Fig. 16. Deformed meshes for various permeability. The boundary is impervious.

In Fig. 17, the fluid flow at the final load step is shown for $k = 1 \times 10^{-7}$ m^2/(pa s). Here, we can see that, although the outer boundary is impermeable, a fluid flow towards the shear band is obtained. This result have been obtained by several others (Loret and Prevost, 1991; Schrefler et al., 1996, 1998), and is due to the dilatation in the shear band which makes the fluid pressure drop in this region.

7. Concluding remarks

In the present paper, we have discussed a FE method that can handle the condition for existence and development of regularized discontinuities in the displacement and the excess pore pressure fields. A key

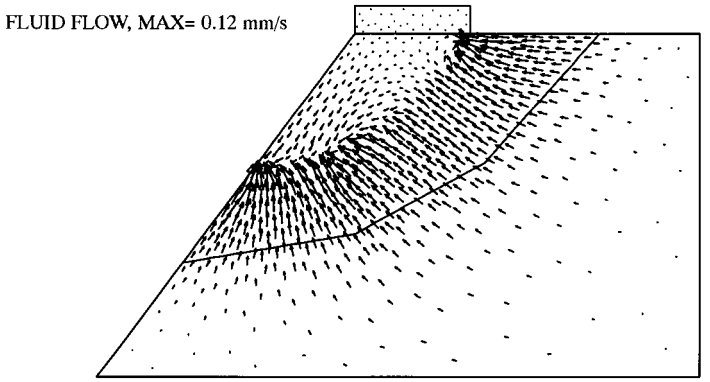

Fig. 17. Fluid flow from the analysis with $k = 10^{-7}$ m^2/(pa s). The results are taken from the final load step.

feature in the establishment of weak equations is the enhanced strain approach (Simo and Rifai, 1990), whereby regularized discontinuities in displacement and pressure can be conveniently embedded in FEs. As a result, besides the global equilibrium and mass balance, local element problems concerning mass balance and traction continuity across the embedded localization band are formulated. It is shown that, under certain circumstances, the element behavior recovers continuum behavior with respect to the discontinuity development (Section 5.3.3).

By a staggering between the continuous structure problem and the discontinuous element problems, an algorithm was developed for the discontinuity evaluation based on loading scenarios. The algorithm can handle situations where onset of localization is preceded by diffuse plastic deformation, and the formulation is shown to work well in terms of the ability to capture localization of skeleton deformation and pore fluid pressure. The orientation of the embedded band is chosen so that its normal coincides with the bifurcation direction of the underlying "effective" material, described by the constitutive law for the effective stress. This choice is made in view of the rate analysis in Larsson and Larsson (2000), where it was concluded that it is the constitutive law for the effective stress that governs the onset of localization. Thus, even for choices of the permeability parameter that corresponds to an almost undrained situation, we do not consider using the orientation for the completely undrained situation (Runesson et al., 1996). Furthermore, the embedded band is positioned within the element in such a way that it goes through the, at the onset, most stressed integration point.

The simulations shows that the FE method has good properties regarding mesh dependence. However, the method is not completely insensitive to the mesh topology. A mesh alignment procedure would probably improve the method in this respect. In the parameter studies the sensitivity w.r.t. local and global drainage conditions is studied. The influence of the friction angle to the localization properties was also studied.

References

Armero, F., Callari, C., 1999. An analysis of strong discontinuities in a saturated poro-plastic solid. Int. J. Numer. Meth. Engng. 46, 1673–1698.

Benallal, A., Comi, C., 1997. Properties of finite-step problem in numerical analysis of unstable saturated porous continua. In: Owen, D.J.R., Onate, E., Hinton, E. (Eds.), Proceedings of COMPLAS V: Computational Plasticity, Fundamentals and Applications. CIMNE, Barcelona, p. 1611–1616.

Coussy, O., 1995. Mechanics of Porous Continua, Wiley, Chichester, England.

De Borst, R., Sluys, L.J., Mühlhaus, H.-B., Pamin, J., 1993. Fundamental issues in finite element analyses of localization of deformation. Engng. Computat. 10, 99–121.

Ehlers, W., Volk, W., 1997. On shear band localization phenomena of liquid-saturated granular elastoplastic porous solid materials accounting for fluid viscosity and micropolar solid rotations. Mech. Cohesive Friction. Mater. 2, 301–320.

Finno, R.J., Harris, W.W., Mooney, M.A., Viggiani, G., 1997. Shear bands in plane strain compression of loose sand. Géotechnique 47 (1), 149–165.

Han, C., Vardoulakis, I., 1991. Plane strain compression experiments on water-saturated fine-grained sand. Géotechnique 41 (1), 49–78.

Kirkebø, S., 1994. A numerical study of excavations in low permeable soils. Ph.D. Thesis No. 1994:28, Department of Geotechnical Engineering, The Norwegian Institute of Technology, University of Trondheim, Norway.

Larsson, J., Larsson, R., 1999. Computational strategy for capturing localization in undrained soil. Computat. Mech. 24, 293–303.

Larsson, J., Larsson, R., 2000. Localization analysis of fluid-saturated elastoplastic porous media using regularized discontinuities. Mech. Cohesive Friction. Mater., in press.

Larsson, R., Runesson, K., 1996a. Element-embedded localization band based on regularized displacement discontinuity. J. Engng. Mech. (ASCE) 122, 402–411.

Larsson, R., Runesson, K., 1996b. Implicit integration and consistent linearization for yield criteria of the Mohr-Coulomb type. Mech. Cohesive Friction. Mater. 1, 1–17.

Larsson, R., Runesson, K., Ottosen, N.S., 1993. Discontinuous displacement approximation for capturing plastic localization. Int. J. Num. Meth. Engng. 36, 2087–2105.

Larsson, R., Runesson, K., Sture, S., 1996. Embedded localization band in undrained soil based on regularized strong discontinuity – theory and FE-analysis. Int. J. Solids Struct. 33, 3081–3101.

Loret, B., Prevost, J.H., 1991. Dynamic strain localization in fluid-saturated porous media. J. Engng. Mech. 117, 907–922.

Needleman, A., 1988. Material rate dependence and mesh sensitivity in localization problems. Comput. Meth. Appl. Mech. Engng. 67, 69–85.

Öberg, A.-L., 1997. Matrix suction in silt and sand slopes – significance and practical use in stability analysis. Ph.D. Thesis, Department of Geotechnical Engineering, Chalmers University of Technology, Sweden.

Panesso, J.M., Stein, E., Steinmann, P., 1998. Localization and failure analysis of fluid saturated cohesive and granular soils. In: Idelsohn, S., Oñate, E., Dvorkin, E. (Eds.), Proceedings of the Fourth World Congress on Computational Mechanics: Computational Mechanics – New Trends and Applications. CIMNE, Barcelona, Spain.

Rankka, K., 1994. In-situ stress conditions across clay slopes – a study comprising seven test sites. Ph.D. Thesis, Department of Geotechnical Engineering, Chalmers University of Technology, Sweden.

Rice, J.R., 1975. On the stability of dilatant hardening for saturated rock masses. J. Geophys. Res. 80, 1531–1536.

Rudnicki, J.W., 1983. A formulation for studying coupled deformation pore fluid diffusion effects on localization of deformations. In: Nemat-Nasser, (Ed.), Proc. of the Symp. on the Mechanics of Rocks, Soils and Ice. ASME, New York, pp. 35–44.

Runesson, K., Peric, D., Sture, S., 1996. Effect of pore fluid compressibility on localization in elastic–plastic porous solids under undrained conditions. Int. J. Solids Struct. 33, 1501–1518.

Schrefler, B.A., Sanavia, L., Majorana, C.E., 1996. A multiphase medium model for localization and post-localization simulation in geomaterial. Mech. Cohesive Friction. Mater. 1 (1), 95–114.

Schrefler, B.A., Zhang, H.W., Pastor, M., Zienkiewicz, O.C., 1998. Strain localization modelling and pore pressure in saturated sand samples. Computat. Mech. 22 (3), 266–280.

Simo, J.C., Armero, F., Taylor, R.L., 1993a. Improved versions of assumed enhanced strain tri-linear elements for 3D finite deformation problems. Comp. Meth. Appl. Mech. Engng. 110, 359–386.

Simo, J.C., Oliver, J., Armero, F., 1993b. An analysis of strong discontinuities induced by strain-softening in rate-independent solids. Computat. Mech. 12, 277–296.

Simo, J.C., Rifai, M.S., 1990. A class of mixed assumed strain methods and the method of incompatible modes. Int. J. Num. Meth. Engng. 29, 1595–1638.

Steinmann, P., 1999. A finite element formulation for strong discontinuities in fluid-saturated porous media. Mech. Cohesive Friction. Mater. 4, 133–152.

Vardoulakis, I., 1996a. Deformation of water-saturated sand: I. Uniform undrained deformation and shear banding. Géotechnique 46 (3), 441–456.

Vardoulakis, I., 1996b. Deformation of water-saturated sand: II. Effect of pore water flow and shear banding. Géotechnique 46 (3), 457–472.